1-1-2010

Abrasive jet micro-machining of metals

Sayeed Ally
Ryerson University

ABRASIVE JET MICRO-MACHINING OF METALS

by

Sayeed Ally, B.Eng.

Ryerson University, 2010

A thesis

presented to Ryerson University

in partial fulfillment of the

requirements for the degree of

Master of Applied Science

in the program of

Mechanical Engineering

Toronto, Ontario, Canada, 2012

Author’s Declaration

I hereby declare that I am the sole author of this thesis.

I authorize Ryerson University to lend this thesis to other institutions or individuals for the purpose of scholarly research.

I further authorize Ryerson University to reproduce this thesis by photocopying or by other means, in total or in part, at the request of other institutions or individuals for the purpose of scholarly research.

Borrower's Page

Ryerson University requires the signatures of all persons using or photocopying this thesis. Please sign below and give the address and date.

Abstract

Abrasive Jet Micro-Machining of Metals

Master of Applied Science, Mechanical Engineering, 2012, Sayeed Ally

Yeates School of Graduate Studies, Ryerson University

Abrasive jet micro-machining is a process that utilizes small abrasive particles entrained in a gas stream to erode material, creating micro-features such as channels and holes.

Erosion experiments were carried out on aluminum 6061-T6, Ti-6Al-4V alloy, and 316L stainless steel using 50 μm Al_2O_3 abrasive powder launched at an average speed of 106 m/s. The dependence of erosion rate on impact angle was measured and fitted to a semi-empirical model.

The erosion data was used in an analytical model to predict the surface evolution of unmasked channels machined with the abrasive jet at normal and oblique incidence, and masked channels at normal incidence. The predictions of the model were in good agreement with the measured profiles for unmasked channels at normal and oblique impact, and masked channels in at normal incidence up to an aspect ratio (channel depth/width) of 1.25. For the first time, it has been demonstrated that the surface evolution of features machined in metals can be predicted.

Acknowledgements

I would like to thank those who gave me the opportunity and means to work on this project. I would like to thank my supervisors Dr. Marcello Papini and Dr. J.K. Spelt for their guidance, perspectives, expertise and understanding, which added considerably to my experience as a graduate student.

I owe gratitude to Joseph Amankrah, Alan Machin and Qiang Li for their technical support during various stages of this research.

I would like to thank The Ministry of Training, Colleges and Universities for financial support through the Ontario Graduate Scholarship (OGS) program.

This Research was supported with funding from the Natural Sciences and Engineering Research Council of Canada (NSERC).

Thanks are also due to Micralyne Inc. and Angstrom Power Inc. for financial and technical support.

Sayeed Ally

Table of Contents

List of Tables

List of Figures

List of Appendices

Nomenclature

The definition of symbols in alphabetical order:

Symbol	Name	Unit
a	Constant	[non-dimensional]
b	Constant	[non-dimensional]
c	Constant	[non-dimensional]
C	Constant	[non-dimensional]
D	Particle diameter	[m]
E	Elastic modulus	[N/m^2]
$E(\alpha)$	Erosion rate an arbitrary impact angle	[mm^3 kg^{-1}], [g/g]
E_{90}	Erosion rate at normal impact angle	[mm^3 kg^{-1}], [g/g]
E_v	Volumetric erosion rate	[mm^3 g^{-1}]
$g(\alpha)$	Normalized erosion rate	[non-dimensional]
h	Standoff distance	[mm]
Hv	Vicker's hardness	[GPa]
k	Velocity exponent	[non-dimensional]
K_{1C}	Fracture toughness	[MPa·m$^{1/2}$]
$k2$	Constant	[non-dimensional]
l	Channel length	[mm]
$n1$	Parametric exponent	[non-dimensional]
$n2$	Parametric exponent	[non-dimensional]
$Q(x)$	Erosive efficacy	[kg·m^{-1}·s^{-2}]
r	Jet spread radius	[m]
t	Time interval	[s]
U_T	Toughness	[N/m^2]
u_e	Specific erosion energy	[J/mm^3]
u_m	Specific melting energy	[J/mm^3]
v	Particle velocity	[m/s]
w	Mask width	[m]
x	Horizontal profile coordinate	[m]
x_i	Experimental profile point	[m]
y	Channel length coordinate	[m]
z	Depth coordinate	[m]
$z_{,t}$	Partial derivative of z w.r.t. time	[m/s]
$z_{,x}$	Partial derivative of z w.r.t. x	[m/m]
z_i	Experimental profile point	[m]

Greek symbols

α	Global impact angle	[deg]
β	Focus coefficient	[non-dimensional]
ϕ	Particle mass flux	[kg·m^{-2}·s^{-1}]
θ	Local impact angle	[deg]
ρ_s	Density of target	[kgm^{-3}]
ε_U	Uniform strain	[-]

Chapter 1: Introduction

1.1 Motivation

Conventional micromachining techniques often are limited by material type or present rather costly solutions. For instance, chemical etching requires significant preparation and processing time, technical knowledge and strict adherence to safety guidelines, in addition to a high capital and operating cost [1 - 3]. The same can be stated for electrochemical machining, which is often limited to conductive materials and requires exorbitant initial investment and high operating cost, including the need for supporting infrastructure such as high output electrical sources [4, 5]. Similarly, electron beam machining requires high capital investment, poses health hazards through the production of x-rays, and cannot be used for machining very small tolerances because its mechanism of removal is vaporization of the substrate [6 - 7].

Abrasive jet micro-machining (AJM) is a relatively new micro-machining technique that utilizes an air jet of small abrasive particles to erode the surface of a material creating micro-features [8, 9]. The AJM apparatus consists of a micro-blaster that combines air and abrasive into a mixture. The stream of abrasive exit a jet, striking the target in a manner controlled by a computer controlled stage, as shown in Figure 1-1. Unlike the aforementioned techniques, the advantages of AJM are its low capital and operating costs, it is an environmentally friendly process that poses no major health hazards, and it has the ability to machine anisotropic and suspended structures on the same substrate [9]. In addition multiple depth features can be machined on the same substrate, unlike chemical etching whereby the entire substrate is etched at a constant rate [10].

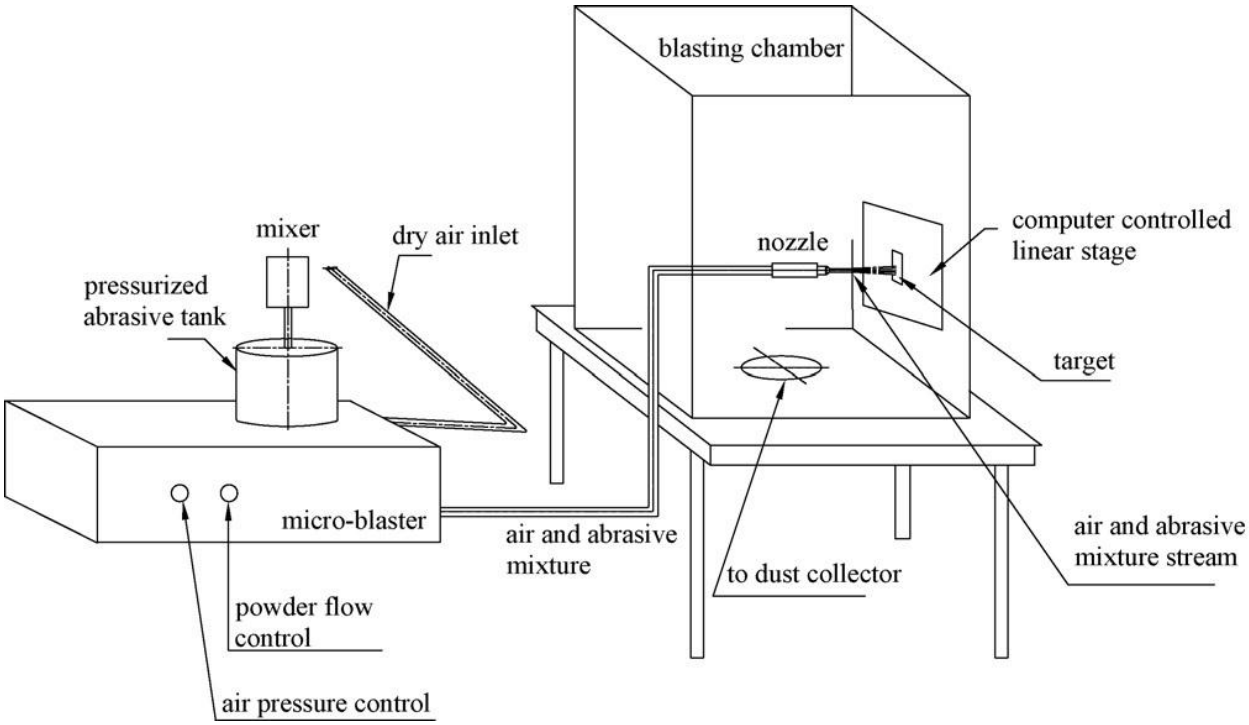

Figure 1-1: The abrasive jet micro-machining experimental apparatus [12].

Typical AJM applications include the drilling, cutting and engraving of glass, ceramics and some hard metals. It can also be used to etch labels in plastics and metals, deburr, deflash and clean materials after conventional machining techniques [8]. The AJM of metals is of particular interest because they represent relatively low cost substrates, are widely available, recyclable, disposable, and offer good strength for structural purposes. Titanium alloys and stainless steel are of particular interest because of their current application in the biomedical industry. Furthermore aluminum alloys are being sought as an alternative to steel and titanium as a lighter material for structural applications. However, most of the research thus far on AJM has focused only on brittle materials such as glass. A notable exception is the work of Park et al. [11], who used the AJM process to machine micro-pockets in stainless steel, while Getu et al. [12 - 14] and Ghobeity et al. [9, 15] developed predictive models for the AJM of polymers. The AJM of metals has significant applications in the micro-machining of channels in micro-fluidic and MEMs devices [16], such as the use of micro-molds to create micro-fuel cells. However, to the knowledge of the author, the AJM of micro-channels has never before been demonstrated in the literature, and there are currently no available models that allow the prediction of the evolving shape and size of micro-features such as channels and holes made using AJM in metals. The main objectives of this thesis aim to address these gaps in the literature.

1.2 Objectives

The main objective of this thesis was to develop and test a model capable of predicting the surface morphology of the cross-section of channels machined using AJM in aluminum 6061-T6, 316L stainless steel, and Ti-6Al-4V alloy. This was accomplished by meeting the following secondary objectives:

i. Determine the erosion rates and erosion mechanisms resulting from blasting 50μm aluminum oxide particles on aluminum 6061-T6, 316L stainless steel and Ti-6Al-4V alloy targets at various angles of attack.
ii. Use AJM to micro-machine unmasked channels at normal (i.e. perpendicular incidence) and oblique incidence, and masked micro-channels at normal incidence, for the same materials and particles described in (i).
iii. Model the surface evolution of the features made in (ii) by modifying existing techniques developed for the AJM of ductile polymers.
iv. Compare the predictions of the surface evolution model to measured cross-sectional profiles from the experiments of (ii).

Chapter 2: Literature Review

Abrasive jet micro-machining involves material removal by impinging solid particles and is thus closely related to solid particle erosion phenomena. In this chapter, a review of the existing literature pertaining to the solid particle of erosion of metals and abrasive jet micro-machining will be presented.

2.1 Solid particle erosion

Solid particle erosion is the loss of material due to the bombardment of a solid surface by small abrasive particles. The particles strike the surface causing material removal through erosion. The extent to which the material is eroded is governed by many experimental parameters, such as material properties, particle properties, and experimental setup. In most cases, there are a few erosion mechanisms responsible for material removal.

Solid particle erosion on metals has been widely researched in past years [11, 19-26]. Many researchers have attempted to model the process, and correlate blast parameters and their effect on erosion. In engineering, solid particle erosion can play either a destructive or constructive role. For example, in helicopter blades used in desert regions, the abrasive wear caused by surrounding sand can be detrimental to the function of the helicopter, and endanger many lives. However, the erosion of metals can also be used in a beneficial manner. For example, micro-features such as micro-channels can be created using a process known as abrasive jet micromachining (AJM). AJM utilizes compressed air to accelerate a stream of abrasive particles to high speed through a nozzle, forming a particle jet that strikes a target substrate. The particles impinge the target surface and mechanically remove material through solid particle erosion mechanisms.

A patterned erosion resistant mask can be used to protect certain parts of the surface from erosion, allowing for the creation of micro-features, such as channels and holes. AJM differs from traditional sandblasting because it uses much smaller particle sizes and a more controlled jet, yielding smaller more refined micro-features. By controlling the jet trajectory and scan speed of the abrasive jet over the erosion resistant mask, various types of eroded micro-features, such as micro-channels, micro-holes, and stepped planar areas, can be created. Surface evolution models have been developed to predict the shapes of masked and unmasked features machined in glass using AJM [9, 15].

AJM has recently been used on polymers such as polymethylmethacrylate (PMMA) [12] and polycarbonate [13]. Most recently, a cryogenic setup was developed to cool the target material, making possible the AJM of elastomers such as polydimethylsiloxane (PDMS) [15]. However, the AJM of metals has only been recently explored. For example, Park et al. [11] utilized AJM to produce micro-mould dies in stainless steel, but they did not attempt to model the process.

2.2 Solid particle erosion mechanisms in metals

Many researchers have extensively studied the erosive characteristics of metals, and the mechanisms that are responsible for material removal. Several opinions exist on which mechanisms govern erosion under varying impact conditions, such as impact angle, particle velocity, material characteristic etc.

There are two fundamental views on the erosion process in metals: the first being a single mechanism phenomenon applicable at all impingement angles, and the second being a superposition of two mechanisms, the latter of which is widely accepted [18].

O'Flynn et al. [26] provided a detailed explanation of the two fundamental mechanisms that govern the erosion of ductile metals, during their quest to correlate material properties with erosion in the development of a model. For metals, a cutting mechanism is found to dominate at lower impact angles while a deformation mechanism is responsible for material removal at higher angles. This contrasts the work done by Morrison and Scattergood [25], who argued that a single erosion mechanism can be operative at all impact angles.

2.2.1 Erosion by cutting

O'Flynn et al. [26] described the cutting mechanism as a means of material removal at lower impact angles while testing twelve different heat treated steels. As a particle impinges upon the surface of a metal, a small crater is dug out as in Figure 2-1a, by the sharp edge between the particle and the substrate. On the back side of the impact site, a highly deformed region is formed as chips, which are subsequently removed by following impacts. Similar mechanisms were found by Singh et al. [24] for 304, 316 and 410 stainless steels.

The amount of damage caused by the cutting and chip formation mechanism is governed by particle and material parameters and the angle of attack. For ductile metals, the angle between the surface of the substrate and the leading face of the impinging particle is defined as the critical angle. Below the critical angle ploughing occurs, and above the critical angle chip formation occurs [26]. The critical angle depends mainly on material properties, namely ductility and work hardening. A higher strain hardening exponent leads to a higher critical angle, and thus less erosion.

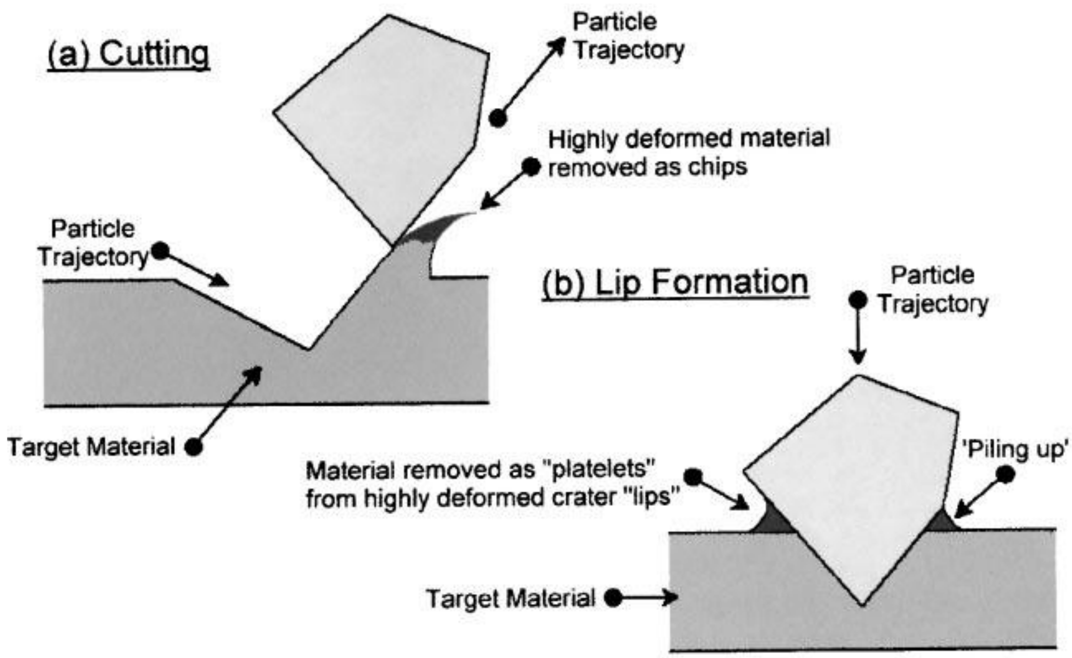

Figure 2-1: Cutting (a) and deformation (b) mechanisms of material removal during solid particle erosion in metals [26].

2.2.2 Erosion by deformation wear

Deformation wear, or indentation, is the mechanism most thought of to govern erosion of metals at normal impact [26]. As the particle strikes the surface, it indents within the surface forming a crater surrounded by highly deformed regions or “lips” (Figure 2-1b). These lips (or material pile up) around the impact zone are formed into platelets and removed when impacted by subsequent particles [22].

The tendency for the platelets to form is also controlled by material properties. The more ductile a material is, the higher tendency there is for the particle to sink in, not causing lip formation, which in turn decreases the erosion rate. A material that is less prone to strain hardening however, forms more platelets which can be removed by subsequent impacts, hence the erosion rate at normal impact may be higher [26].

2.2.3 Single mechanism of erosion

While major contributors to the solid particle erosion of metals research field have observed that erosion is caused by the superposition of two mechanisms, cutting and deformation, some authors have nevertheless claimed that one single erosive mechanism occurs at all angles.

In the investigation of the erosion of 304 stainless steel, Morrison and Scattergood [25] noted that the surface morphology of the stainless steel blasted with 37 – 270 µm angular alumina particles were quite similar at normal and oblique impacts. They argued that a single mechanism of erosion was dominant at all angles because there was no evidence indicating a change in surface morphology, and furthermore the velocity and particle size dependence of erosion as a function of angle of attack did not vary as much to warrant a dual mechanism explanation.

It was then concluded that one mechanism, which includes cutting, ploughing and deformation is linked to shear deformations that control material displacements within a process zone [25]. This mechanism must be operative at all impact angles, as shown in Figure 2-2.

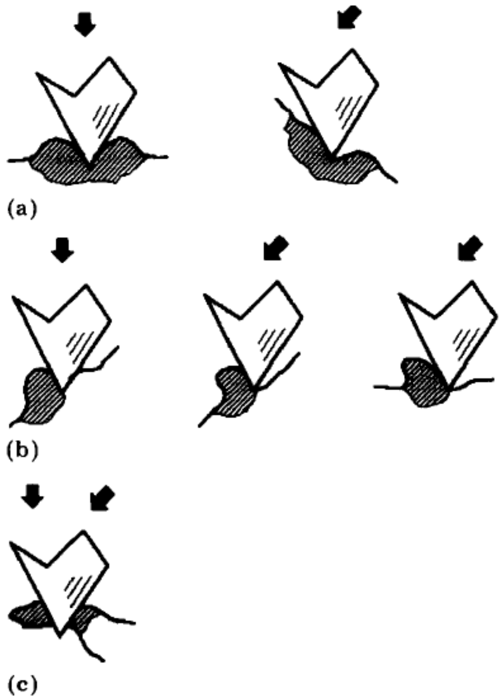

Figure 2-2: A schematic diagram showing impact events on various surfaces: (a) indentation, (b) ploughing, and (c) platelet cutting. Arrows indicate direction of impact, and shaded regions indicate the process zone deformation [25].

2.3 Particle parameters affecting erosion in metallic materials

2.3.1 Impact angle dependence on erosion

It has long been known that the erosion of ductile metals depends strongly on the angle of impact, α, of the abrasive particles, as defined in Figure 2-3. Many authors have suggested (e.g., [18, 24, 25]) that most ductile materials eroded by angular particles exhibit a peak erosion rate in the range of 20 - 45°, while brittle materials peak at a maximum of 90°. The dependence of erosion on impact angle leads back to the discussion on the fundamental mechanisms governing erosion.

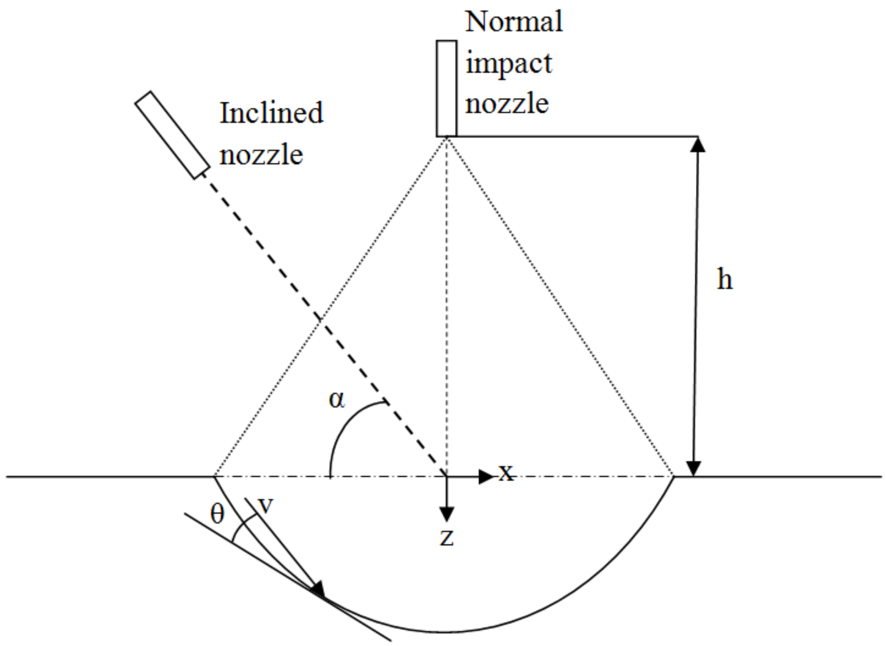

Figure 2-3: The global impact angle, α, and local impact angle θ of an inclined abrasive jet.

During erosion at low angles of attack, the horizontal component of velocity is responsible for chip formation and eventually removing material by the cutting mechanism. Ductile materials erode more at these angles, since their failure mechanism is in shear. Materials being attacked at angles approaching normal are repeatedly deformed until platelets or cracks are formed (as in the case of brittle materials). Since most metals are ductile, it is expected that the maximum erosion rate will occur at an oblique angle, when the horizontal component of the velocity has a non-zero value.

To name but a few, Oka et al. [18, 27], Morrison and Scattergood [25], Yerramareddy and Bahadur [22], Rodriguez et al. [28], and Harsha and Bhaskar [23], have all reported an erosion dependence of metal on impact angle. For ductile materials, it is found that peak erosion occurs at some angle – other than 90° – and then tapers off at nearly glancing. There are a number of experimental parameters, such as material hardness, particle shape and velocity [29] that may affect the erosion dependence on angle for metals.

Oka et al. [27] considered modeling this impact angle dependence of erosion (Figure 2-4) by using a trigonometric function. Other attempts were made at modeling this by O’Flynn et al.

[26] (by using an equation combining the cutting and deformation components), and by Shipway [30] (also by a trigonometric function). Neilson and Gilchrist [20] also predicted the erosion-angle of attack characteristics on various surfaces.

Presented below are the findings of Oka et al. [18, 27]:

The impact angle dependence of erosion, $E(\alpha)$ is given by:

$$E(\alpha) = g(\alpha)\ E_{90} \tag{2-1}$$

where E_{90} is the erosion rate at normal impact, and the normalized impact angle dependence of erosion, $g(\alpha)$, is given by the product of a plastic deformation and a cutting term [18]:

$$g(\alpha) = (\sin\alpha)^{n1}\ (1 + Hv\ (1-\sin\alpha)^{n2} \tag{2-2}$$

where n_1 and n_2 are experimentally determined exponents and Hv is the initial target hardness. Eq. (2-2) is a trigonometric estimation of the erosion rate dependence on angle, with the first factor being related to the plastic deformation (impact energy normal to surface) while the second term is related to the cutting action (impact energy parallel to surface) [12].

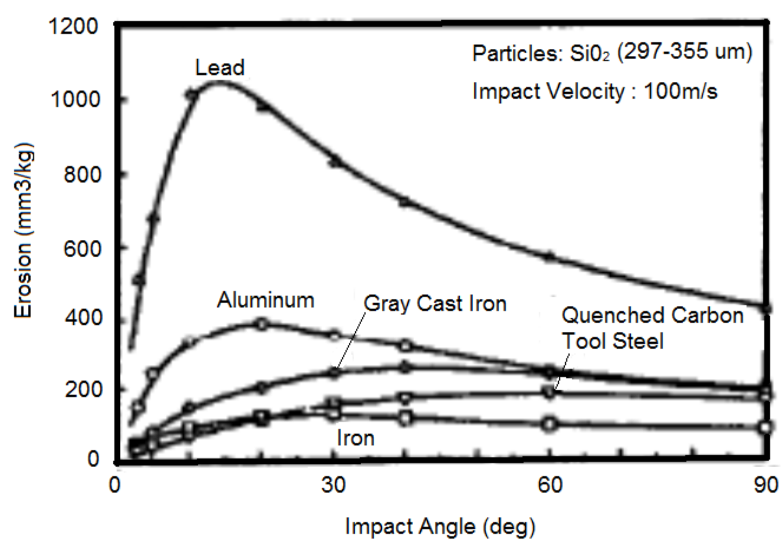

Figure 2-4: Erosion rate of different metals as a function of angle of attack [18]. The fit of the lines are governed by Eq. (2-2).

Oka et al. [18, 27] were able to semi-empirically model the angular dependence of erosion rate fairly accurately (Figure 2-4). In addition, the model predicted a peak in the erosion rate as a function of angle, *E(α)*, (unlike that of O' Flynn et al. [26]), and scaled well with the increase in erosion rate from normal impact to oblique impact angles for ductile materials. As Figures 2-4 and 2-5 indicate, the considerable increase in the erosion rate between the maximum oblique angle of attack for ductile materials and normal impact is approximately double. Thus it can be concluded that the erosion rate's dependence upon the impact angle during solid particle erosion is significant.

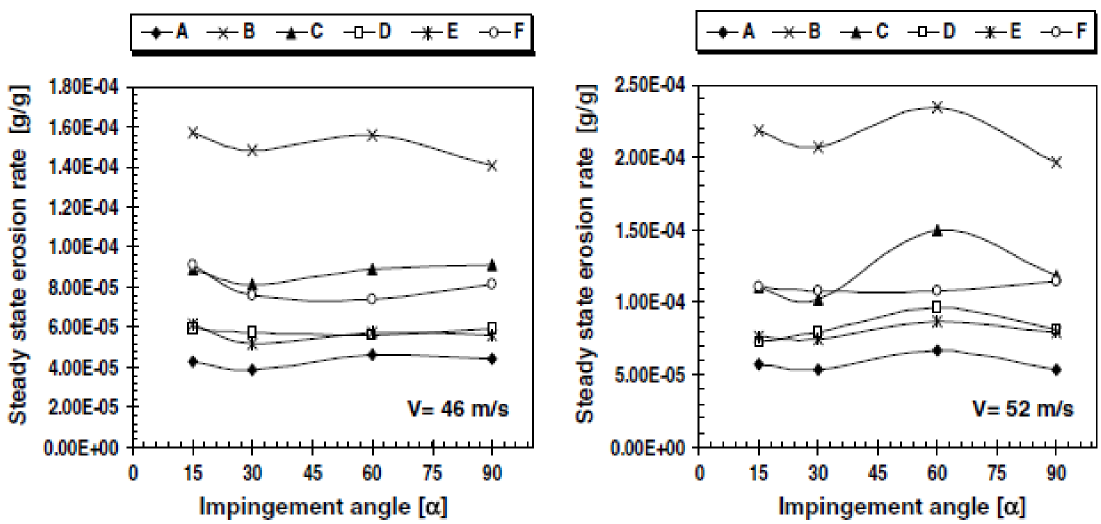

Figure 2-5: Impact angle dependence on the erosion of ferrous and non-ferrous materials at 46 m/s (a) and 52 m/s (b) [23]. A = aluminum, B = brass, C = copper, D = mild steel, E = stainless steel and F = cast iron.

2.3.2 Particle size

The size of particles used in the erosion process can affect the erosion rate by affecting the resulting amount of damage and the type of mechanism governing the erosion. For metals, larger particles tend to do more damage than smaller ones, however there is a threshold. Morrison and Scattergood [25] noted the erosion rate tended to increase when eroding 304 stainless steel with alumina abrasive particles as the particle size increased, until a particle size of 130 µm, after which the erosion rate leveled off. Figure 2-6 illustrates this particle threshold limit.

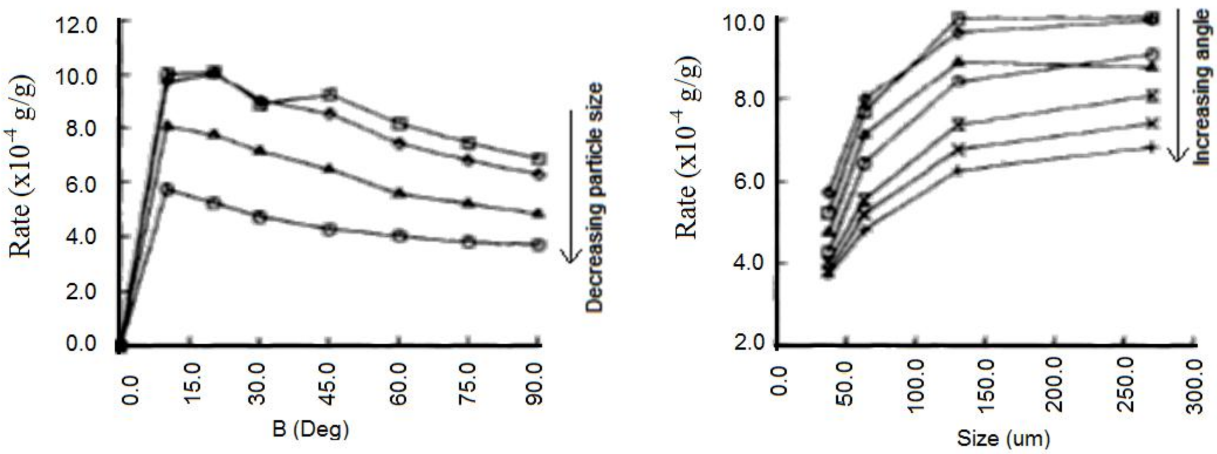

Figure 2-6: The erosion rate at different angles for varying particle sizes (left). Erosion rate versus particle size (right), with increasing angle as the curves decrease [25].

As Figure 2-6 shows, the particle size does not affect the relative dependence of erosion rate on the impact angle, but only its magnitude, as the shape of the erosion versus impact angle curves remain very similar as the particle size changes.

A similar particle size threshold at 50 µm was found by Yerramareddy and Bahadur [22] when eroding Ti-6Al-4V alloy with silicon carbide particles. Generally, it was found that the erosion rate below 50 µm was found to be proportional to $D^{2/3}$, where D is the particle size. It was concluded that smaller particles cause more deformation (and thus less erosion for ductile metals), while for larger particles the predominant mechanism is cutting.

2.3.3 Particle velocity

Erosion of metals is highly influenced by the velocity of the particles upon impact. It has generally been accepted that the relation between particle velocity and erosion rate is governed by $E = Cv^k$ [25], where E is the erosion rate, v is the particle impact velocity, and k is the velocity exponent.

Oka et al. [18] and Yerramareddy and Bahadur [22] observed that the value of k is between 2 and 3 for ductile metals, and between 3 and 5 for brittle metals [23]. Figure 2-7 shows the relation between erosion rate and velocity for a typical ductile metal.

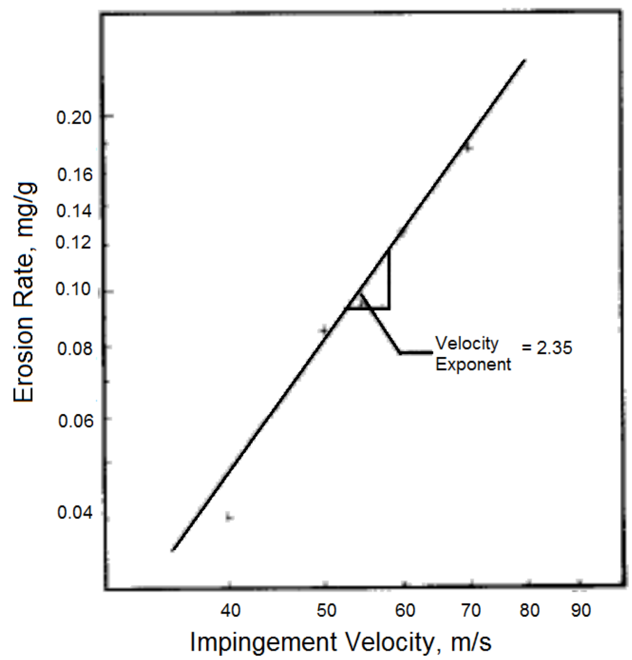

Figure 2-7: Erosion rate versus velocity for a typical ductile Ti-6Al-4V alloy, plotted on a log scale [22]. The velocity exponent $k = 2.35$.

Some investigators have reported that the velocity exponent, k, varies with the angle of attack. For example, Finnie and McFadden [31] found k increases from 2.46 to 3.16 when angles were increased from 10° to 80° for the erosion of 1100-O aluminum by SiC particles. In contrast, Morrison and Scattergood [25] found that the velocity exponent is independent of impact angle within experimental error when eroding 304 stainless steel, which was similar to what was found by Oka et al. [27]. However, the value of the velocity exponent decreased with an increase in the erodent particle size, which could be attributed to a temperature rise during particle impact [25].

Oka et al. [27] found that impact velocity and particle size were independent of each other relative to the dependence of E_{90}. The particle size did not affect the velocity dependence of erosion, nor did the velocity affect the particle size dependence of erosion. It was found that other particle properties and material hardness played a more significant role in this regard.

2.3.4 Particle type

The type of particle, whether spherical or sharp angular, can cause a substantial change in the erosion mechanism and thus a change in the erosion rate of a metal. In general, the use of spherical particles was found to cause a shift in the angle of maximum erosion, toward 90°, i.e. normal impact. Cousens and Hutchings [32] found low carbon steel exhibited a maximum erosion rate at 90°, when eroded by glass spheres instead of a typical ductile erosion maximum of 20° when eroded by SiC or sharp glass. Sapate and Rama Rao [29] also found that harder alumina particles 125 - 150 µm in size eroded 1.3 times more than 100 - 150 µm sized SiC particles.

It seems in fact that the sharper particles cause more damage [22] because of their shape which results in a greater penetration in a soft ductile substrate. Thus the mechanisms of erosion will be affected by the particle shape, causing a shift in the magnitude of erosion, as shown in Figure 2-8.

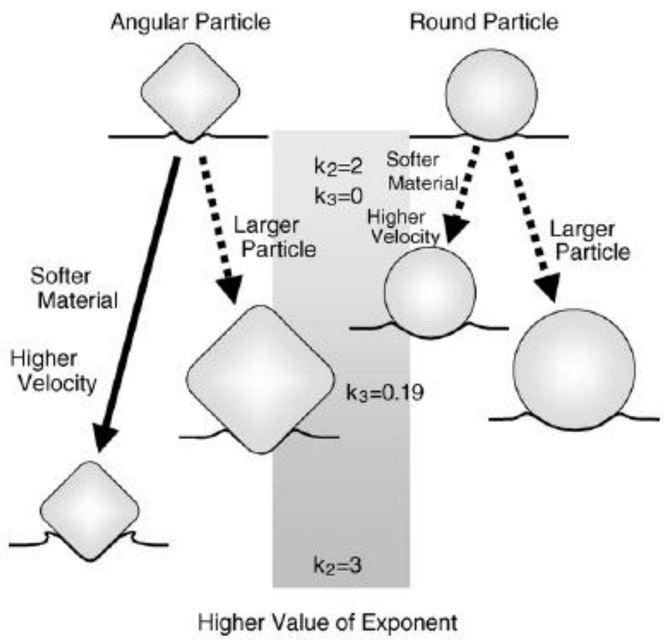

Figure 2-8: The effect of particle type and size on erosion. [27]. Sharper, faster particles tend to penetrate the surface more than rounded, slower particles.

2.3.5 Particle Embedding

Particle embedding during abrasive jet micro-machining is important because the resulting surface finish can affect the performance of the final product. For example, embedded particles could create imprints if the final product was to be used as a micro-mold. Depending on the application, the roughness, hardness and perhaps material properties can be affected by embedding, and thus a quantitative measurement of embedded particles is often required. Morrison and Scattergood [25] used alumina particles ranging from 37 - 270 µm to erode 304 stainless steel samples. However they were unable to find embedded particles. In contrast, Neilson and Gilchrist [20] used 210 µm aluminum oxide particles to erode aluminum substrates at 90°. Since weight loss measurements were used, an initial drop in the erosion rate below zero, or a weight gain by the initial embedment of particles, was detected. A weight loss versus dosage graph is shown in Figure 2-9. Remarkably, when spherical 475 µm glass spheres were used on aluminum, no such deposition effects were observed [20].

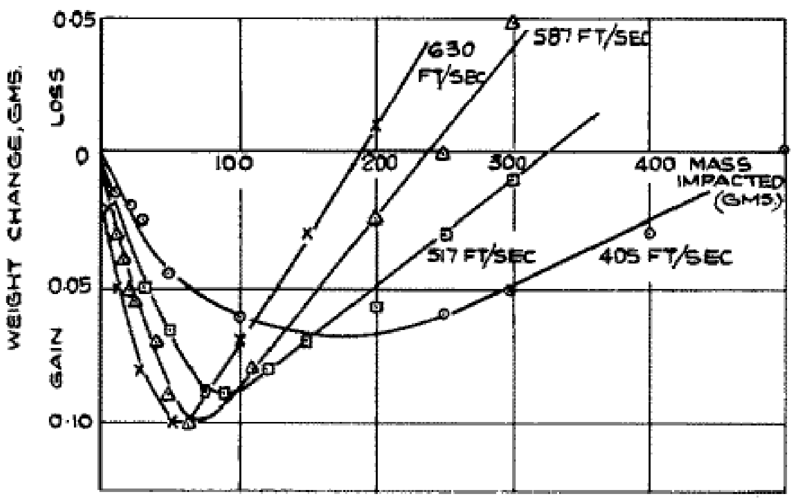

Figure 2-9: Weight loss vs. mass impacted for aluminum plates at various velocities impacted by 210 µm particles at 90°. An initial weight gain is attributed to particle embedding [20].

Harsha and Bhaskar [23] eroded six different metals using 150 - 300 µm silica sand. Sand particles were easily spotted embedded in the surface of aluminum after erosion, as shown in the S.E.M. image in Figure 2-10. Interestingly, Emiliani and Brown [21] noted that the entire surface of a Ti-6Al-4V substrate eroded with 210 µm spherical glass particles was coated with a “glassy layer". This layer was said to be caused by the glass abrasive melting upon impact, protecting the titanium alloy being further eroded.

Figure 2-10: Scanning electron microscope image of aluminum eroded by sand at an angle of 60° and at a speed of 52 m/s [23]. An embedded sand particle is circled.

From the above evidence of particle embedding, the importance of quantifying particle embedding during solid particle erosion is evident. It is seen that material properties, particle type and size are a few factors that affect particle embedding in metals.

2.4 Material Properties Affecting Erosion in Metallic Materials

Many researchers have attempted to relate the hardness of metals to erosion resistance. However, in recent years it has been generally accepted that hardness is not the sole material property that affects erosion; rather it may be another property or a combination thereof. Meng and Ludema [33] found in an analysis of current wear models and predictive equations that hardness and material density were perhaps the two most sought after properties used by researchers to relate material properties to erosion. What is found generally in the literature tends to conclude upon a certain class, range, type, or selection of metals, and any form of a relationship or model presented can rarely be brought forth for general conclusions on other metals. What follows is a brief discussion on some of the material properties known to affect the solid particle erosion of metals.

2.4.1 Hardness

Material hardness was once thought to be the fundamental factor affecting solid particle erosion of metals. Hardness is the resistance of a metal to change shape when penetrated by an object, which in this case is a particle. Thus the hardness of a metal controls how much the impinging particle can penetrate, and depending on the mechanism of material removal discussed previously, the amount of metal that is removed.

Many authors have studied the effect of hardness on the erosion of metal by solid particle bombardment, notably Oka et al. [18, 27], Sapate and Rama Rao [29], and Rodriguez et al. [28]. They have generally found a decrease and/or a shift toward normal in the angular dependence of erosion rate curve with an increase in material hardness.

Sapate and Rama Rao [29] investigated the effect of material hardness on wear for some weld- deposited alloys. Samples with hardness ranging from 300 – 800 *Hv* were eroded with 125 - 150 µm alumina particles and 100 - 150 µm silica sand at varying angles of attack. Figure 2-11 shows a typical plot of impact angle versus erosion for various weld–deposited alloys with varying hardness. The first three metals exhibit typical ductile erosion (peak at 30°), while the fourth alloy exhibits a harder martensitic structure, and thus its peak erosion occurs around 60°. The last two alloys consist of hard second-phase carbide particles which make the alloy extremely hard [29]. It is evident that as the hardness increases, there tends to be more of a shift in the maximum erosion rate toward 90°, signifying a transition to brittle erosion.

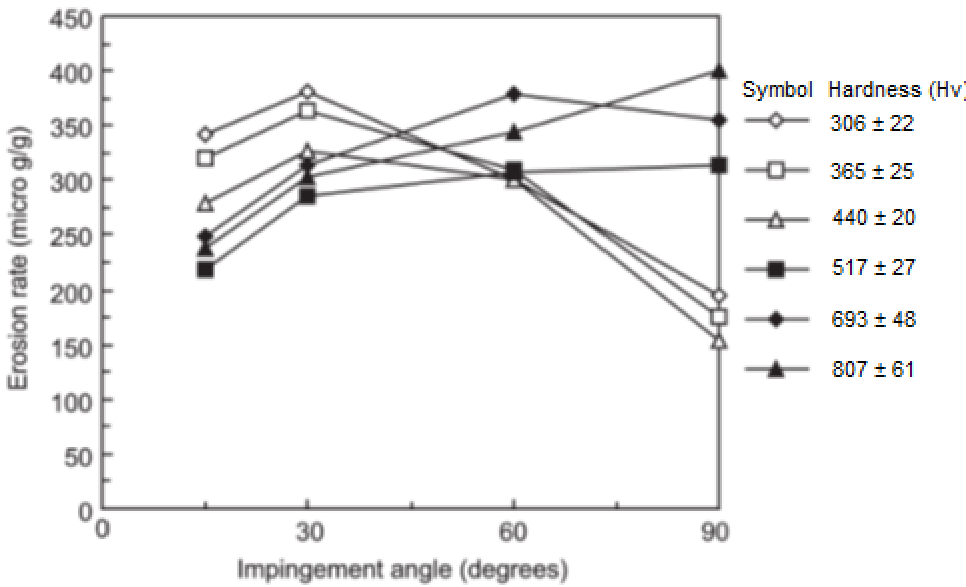

Figure 2-11: The impact angle dependence of erosion for weld-deposited alloys of varying hardness eroded with 125 - 150 µm alumina particles at 50 m/s [29].

Figure 2-12 shows the erosion rate of some weld-deposited alloys plotted against Vickers hardness [29]. For both SiC and alumina abrasive, it can be concluded on a general basis that as the material hardness increases, an increase is sought in the erosion resistance of a metal. However, Sapate and Rama Rao [29] noted that while the erosion rate is inversely proportional to the material hardness, it becomes less sensitive to material hardness if the hardness of the erodent particles is increased. Figure 2-12 reflects this with the harder alumina having a smaller change with increase in material hardness than the silica sand.

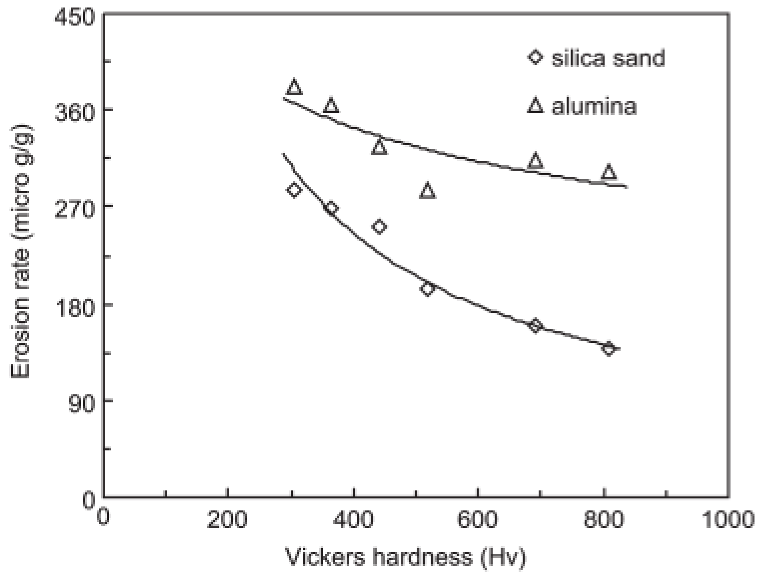

Figure 2-12: Erosion as a function of material hardness for weld-deposited alloys using 100 - 150 µm silica sand and 125 - 150 µm alumina particles at a velocity of 50 m/s [29].

A transition from ductile to brittle erosion as material hardness increases has been noted by Rodriguez et al. [28]. They eroded AISI H13 and 4140 steels with silica sand erodent ranging from 150 - 425 µm. As the hardness increased, a shift, particularly for the H13 steel, was noted in the angle of maximum erosion. The results are presented in a 3-D chart in Figure 2-13, which plots erosion against hardness and impact angle for H13 steel.

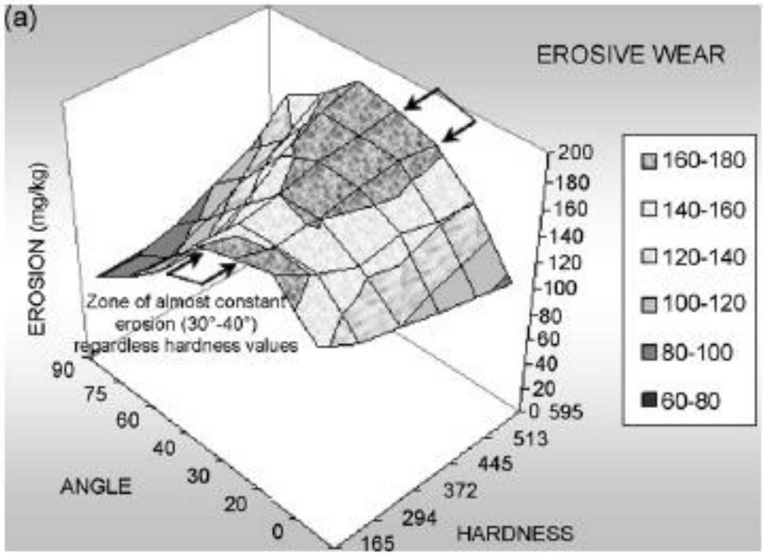

Figure 2-13: Erosion rate as a function of hardness and impact angle for H13 steel eroded by silica sand [28].

Rodriguez et al. [28] noted three distinct zones in the erosion curves: between 10 – 20°, the higher the hardness, the lower the erosion; between 20 – 30 $^{\circ}$, erosion remained constant with increasing hardness; and at angles of 60° and higher, higher erosion was observed with increasing material hardness signifying brittle erosion. The latter was said to be caused by the formation of adiabatic shear bands which create sites for the nucleation and propagation of cracks, reminiscent of brittle erosion.

While attempting to model the erosion in metals, Oka et al. [27] found similar results yet again, with a decrease in the erosion rate as the hardness increases for different types of stainless steels. This hardness relationship was reflected in their model (Eq. 2-2) with the exponents n_1 and n_2, which increase and decrease linearly (on a logarithmic scale) respectively, with hardness. It was found that these exponents are related to hardness for a wide range of hardness, for aluminum, iron and carbon steels. On the contrary, Reshetnyak and Kuybarsepp [34] observed that the relationship between hardness and erosion resistance in hard metals (such as WC-Co) differs substantially from the (somewhat linear) relationship for metals.

2.4.2 Strain hardening

Strain hardening, also characterized by ductility, is the strengthening of a material by plastic deformation, and has an effect on the erosion of metals. The more ductile a material is the more likely and easier it is to plastically deform before fracture. O'Flynn et al. [26] found that the erosion of metals is inversely proportional to the toughness multiplied by the strain to fracture, ε_u, where ε_u is a measurement of strain hardening. Thus it is expected that as the strain hardening exponent increases, a corresponding decrease in the erosion rate occurs.

A similar effect was found by Yerramareddy and Bahadur [22] who investigated the erosion of Ti-6Al-4V alloy using SiC particles. An inverse relation was found between the erosion rate and ductility of the material.

Singh et al. [24] investigated the erosion of 304, 316 and 410 stainless steel and found the lack of strain hardening to have a significant role in the notably higher erosion of the 304 and 316 stainless steel over the 410, which exhibited a soft zone. The abrasive was 160 µm SiC particles. It was found that surface hardening, as a result of strain hardening occurred in 304 and 316, but not 410 stainless steel. An example is shown in Figure 2-14 for 316 stainless steel at 30° and 90°.

The parameter, Hv_{20} / Hv_b, was used to measure the hardness 20 µm below the eroded surface (Hv_{20}) relative to the original surface hardness (Hv_b). 304 and 316 stainless steels exhibited substantial strain hardening, with this factor greater than unity, while the 410 stainless steel had a factor less than one with its known lower ductility and strain hardening ability. Numerically however, Singh et al. [24] were not able to establish a direct relation between erosion and the strain hardening exponent, *n*.

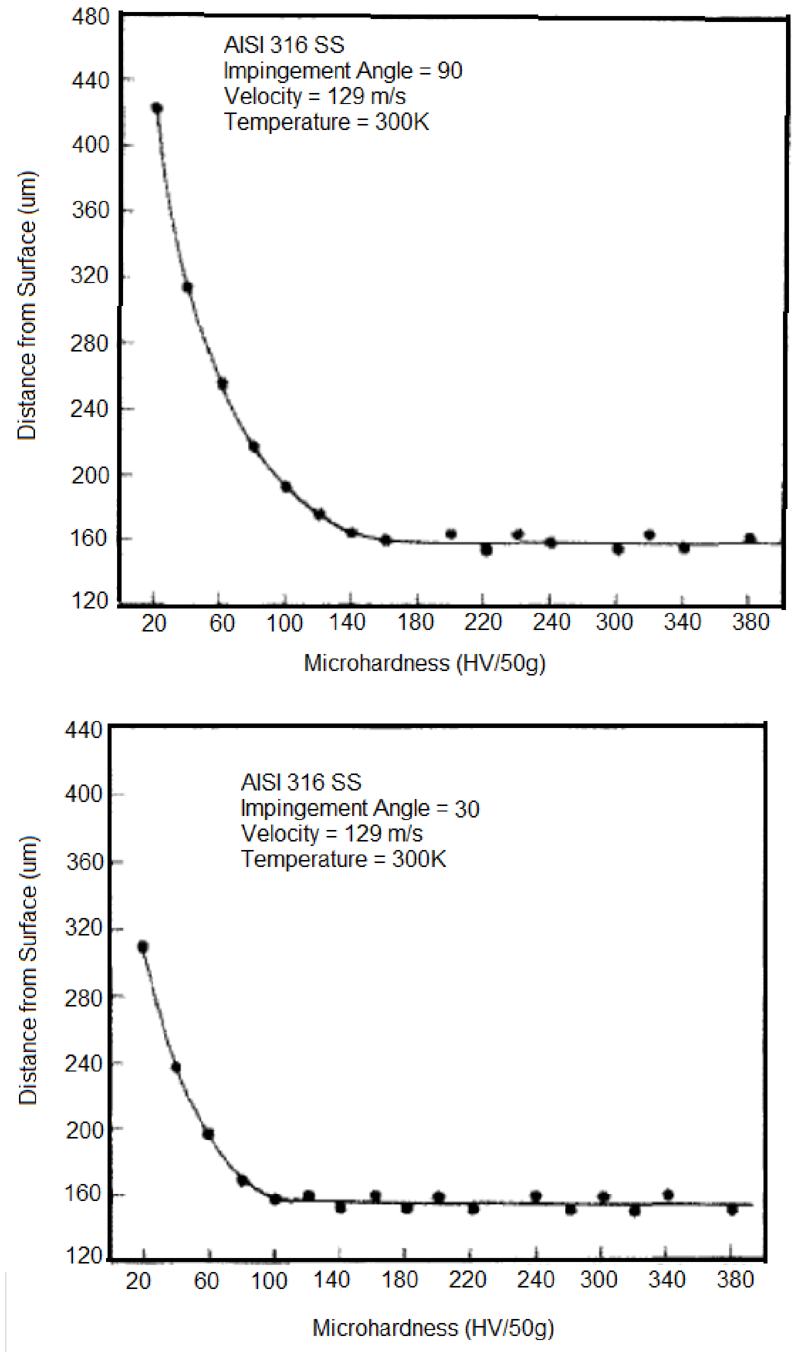

Figure 2-14: Micro-hardness as a function of depth after the erosion of 316 stainless steel [24] at 90° and 30°.

Harsha and Bhaskar [23] also found a considerable increase in the surface hardness after erosion at 90° for ferrous and non-ferrous metals. This was due to substantial strain hardening, as demonstrated in Figure 2-15.

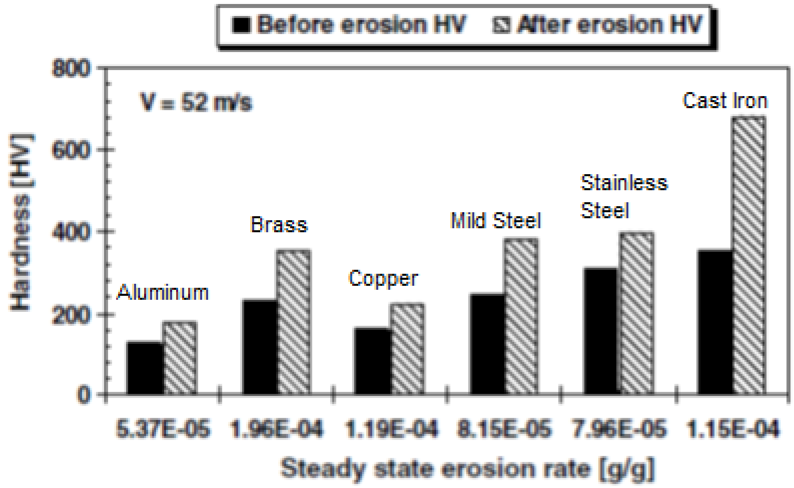

Figure 2-15: Hardness versus erosion rate for various metals eroded by silica sand [23]. A substantial increase in surface hardness was found after erosion signifying strain hardening.

2.4.3 Material Strength

The properties of material strength such as yield strength, ultimate tensile strength or elastic modulus are all derived from a simple tensile test. There has been some investigations carried forth in determining if any relationship exists between the solid particle erosion of metals and these properties. The results, however, are rather mixed, with a general trend indicating no direct correlation between material strength and erosion resistance. To highlight this point, Table 2-1 summarizes the properties of six metals in their order of erosion rate from the work of Harsha and Bhaskar [23] who used 150 - 300 µm silica sand as an erodent.

Table 2-1: Material properties of metals in order of their erosion resistance (derived from [23]).

Mechanical Property / Metal tested in order of erosion resistance	**Aluminum (IS 737)**	**Stainless Steel (IS 410)**	**Mild steel (IS 226)**	**Cast iron (IS 210)**	**Copper (IS 4171)**	**Brass (IS 319)**
Yield strength (MPa)	350	310	240	-	348	395
Ultimate tensile strength (MPa)	460	517	410-580	152	421	485
Elastic modulus (GPa)_	72	200	-	66-97	110-120	96-110
Density (Kg/m^3)	2700	7740	7850	7250	8900	8450
Elongation at break (%)	10	25	23	-	18	20

From Table 2-1, with aluminum having the lowest erosion rate while brass has the highest, it is evident that the main properties (yield and tensile strength, elastic modulus and elongation at break) have no direct correlation to the erosion rate. Yerramareddy and Bahadur [22] also found a similar disconnection between the strength properties when eroding Ti-6Al-4V alloy with SiC particles at 30°. In addition, Yerramareddy and Bahadur [22] concluded that a general inversely proportional relationship was held between the percentage area reduction (ductility) and the erosion rate.

Ambrosini and Bahadur [35] found that an increase in ultimate strength led to an increase in the erosion rate when eroding AISI 4140 steel using 125 μm SiC abrasive. However no correlation between the tensile toughness or impact strength was found, as shown in Figure 2-16.

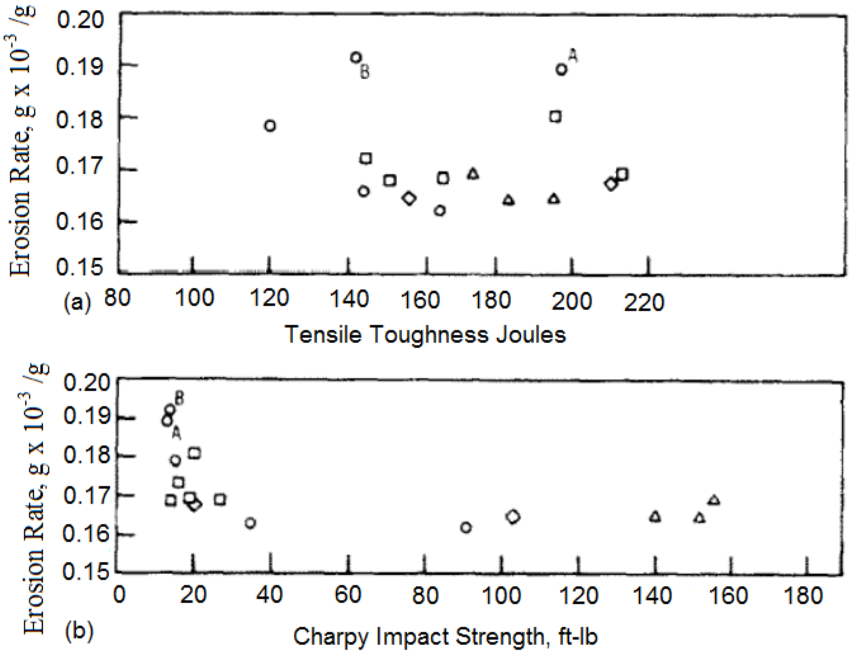

Figure 2-16: Erosion rate versus tensile toughness (a) and Charpy impact strength (b) for AISI 4140 steel [35]. No correlation is found.

Singh et al. [24] could not find a relation between the ultimate tensile strength, yield fracture strain, uniform strain, or the strain hardening exponent to explain their erosion data for 304, 316 and 410 stainless steels.

2.4.4 Toughness and uniform strain to failure

In some models, it is assumed that the volume of the material removed depends primarily on the toughness of a material. Toughness (U_t) is defined as the deformation energy per unit volume of material removed required to produce fracture. It is calculated as the entire area underneath the true stress-strain curve [26], and naturally takes into account the ultimate tensile stress and fracture stress involved during large deformations of material.

Uniform strain (ε_u), also thought to be a governing factor [26] in the erosion of metals, is defined as the amount of strain required to cause the material to neck during a tensile test. Since for ductile metals, uniform strain is also proportional to the strain hardening exponent, it is thus a direct measure for strain hardening capacity, which plays a significant role in the erosion of metals (refer to section 2.4.2 on strain hardening).

O'Flynn et al. [26] was able to inversely relate the product of above two parameters to the erosion rate. However, the model, while composed of cutting and deformation components similar to that of Oka et al. [18], showed only general agreement with experimental data when various heat treated steels were eroded and high temperature material properties were used. They claimed the elevated temperature properties were needed due to the potential localized heating that is caused during the solid particle bombardment of the surface. Nevertheless, while the model could use some improvement, the general relationship established for the erosion rate was $E \alpha 1/(U_T\varepsilon_U)$, which is shown in Figure 2-17.

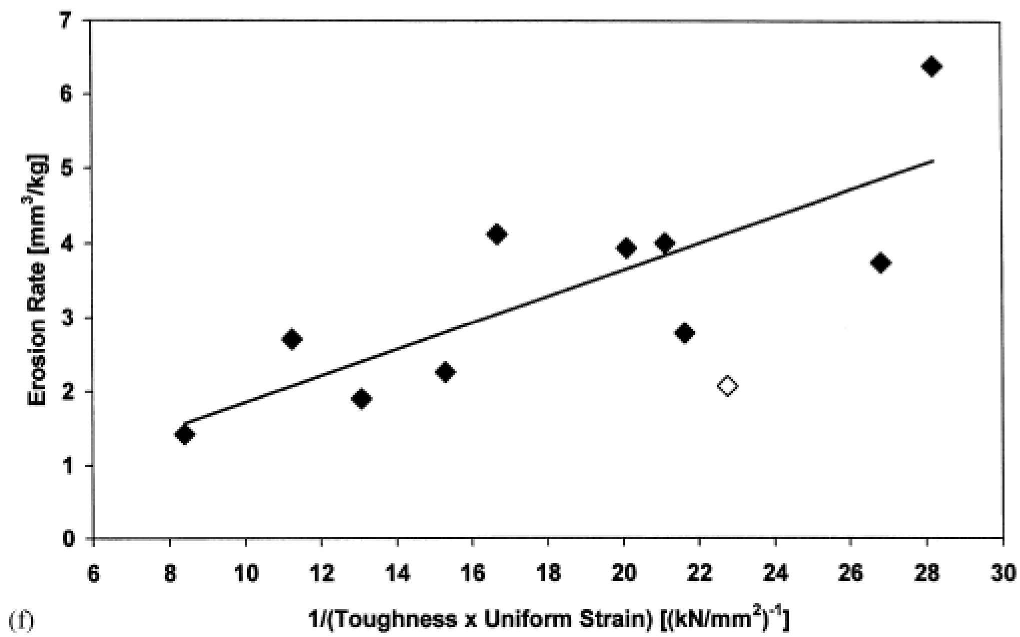

Figure 2-17: The linear relationship between erosion rate and $1/(U_T\varepsilon_U)$ using elevated temperature mechanical properties test data (200°C) for various heat treated steels eroded at an impact velocity of 25 m/s at an angle of 90°. [26]

2.4.5 Other properties

There are some other properties worth mentioning that have been related to erosion in metals. Oka and Yoshida [36] found some materials followed a relationship between E_{90} and the load relaxation ratio. It was found that the erosion rate is associated with the initial plastic deformation characteristics or brittleness of a material. However, the relationship did not hold for some materials due to the differences between the quasi-static indentation testing and actual dynamic erosion tests.

Malkin [37] looked at the erosion process from an energy standpoint. The specific erosion energy, defined as the kinetic energy of the particles per unit volume of material removed, relates linearly to the melting energy. This is due to the large stains and strain rates encountered during solid particle erosion that lead to near adiabatic plastic deformation of the metal to its melting energy limit. In addition, Malkin [37] proved that this relationship worked for a wide variety of metals at different impact speeds, although it is limited to oblique impact cases only. Figure 2-18 shows a typical relationship between specific erosion energy and melting energy for various metals.

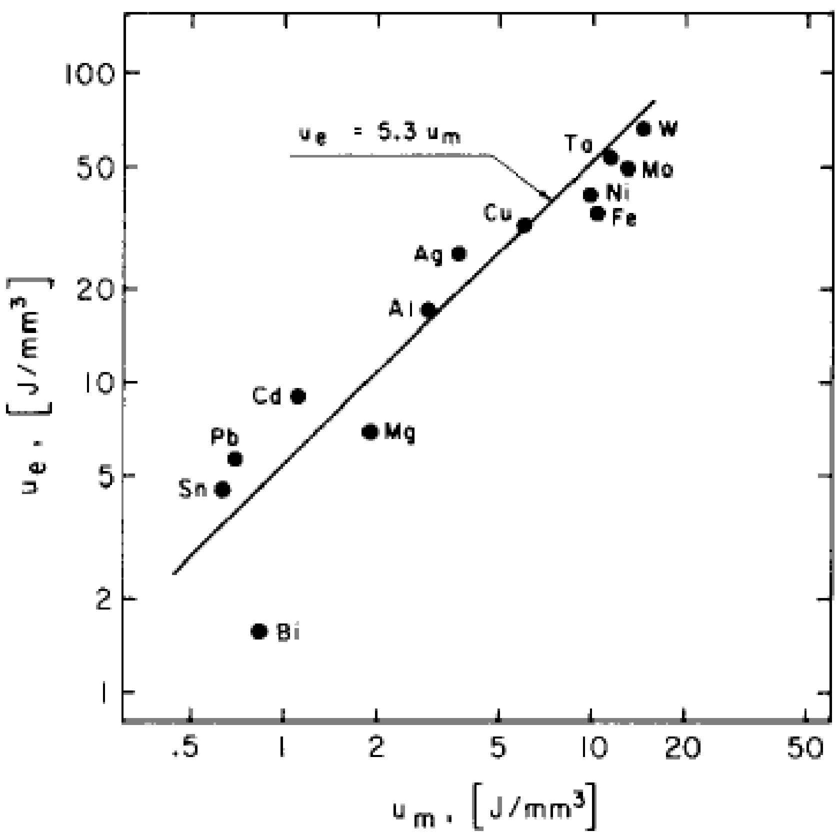

Figure 2-18: Specific erosion energy u_e versus specific melting energy u_m for various metals eroded by SiC particles at 20° at a speed of 76 m/s [37].

2.5 Summary

As a general consensus, the two governing erosion mechanisms are cutting and deformation. Cutting occurs at lower angles of particle impingement, while repeated deformation causes erosion at angles approaching normal [18]. The main factors influencing the erosion of metals are particle parameters and material parameters, as discussed previously.

The size, type and shape of the stream of impinging particles have an adverse effect on erosion. Generally, larger, harder and sharper particles caused more erosion than softer, rounded ones. Erosion relates to velocity via an exponential relationship with velocity exponent ranging between 2 to 3 for ductile metals [23]. There is a substantial dependence of erosion on the particle impingement angle for metals, with maximum ductile erosion occurring at angles between 20 - 45° [18].

Material hardness was found to be the most significant material property affecting erosion on metals. Generally as hardness increased, a corresponding decrease and shift toward normal in the erosion–impact angle relationship was observed. As Table 2-1 showed, other mechanical properties were found to be only vaguely related to the erosion rate. Unfortunately, the models or relationships established in literature could not in general be applied to a wider range of metals or experimental setups other than what was experimented with. Therefore, the relationship with between material properties and erosion could thus be some unknown combination of material properties yet to be discovered [27].

Chapter 3: Experiments

Modeling the surface evolution of the cross-sectional profile of the aluminum, stainless steel and titanium alloys requires knowledge of the dependence of the erosion rate on the angle of attack. This chapter presents solid particle erosion and AJM experiments that were carried out to determine the erosion rate, its dependence on the impact angle, and experimental cross-sectional profiles of micro-machined channels.

3.1 Experimental apparatus

All experiments were performed using an AccuFlo AF10 Micro-Abrasive Blaster, (Comco, Inc. Burbank, CA, USA). A mixing device was used to stir the abrasive mixture to prevent particle agglomeration, and ensure a repeatable mass flux [10], as shown in Figure 3-1. The 50 µm aluminum oxide particles were blasted through a stationary 0.76 mm diameter nozzle using a blasting pressure of 400 kPa. The average speed of the particles in the jet was calculated to be approximately 106 m/s using the model of ref. [39]. Sheets of 6061-T6 aluminum, Ti-6Al-4V alloy and 316L stainless steel were cut into 2.54 x 7.62 x 0.95 cm thick specimens, which were then mounted on a programmable computer controlled linear stage having a positioning accuracy of 0.5 µm (Figure 3-2). The nozzle was attached to a rotating mount and a manual stage which allowed variation of the angle of attack, while holding the nozzle to target standoff distance (along the nozzle centerline) constant at 20 mm (Figure 3-3).

Figure 3-1: The micro-blaster, with mixing device attached atop.

Figure 3-2: The programmable stage to which the metal specimen was mounted. The nozzle was held stationary 20 mm from the substrate.

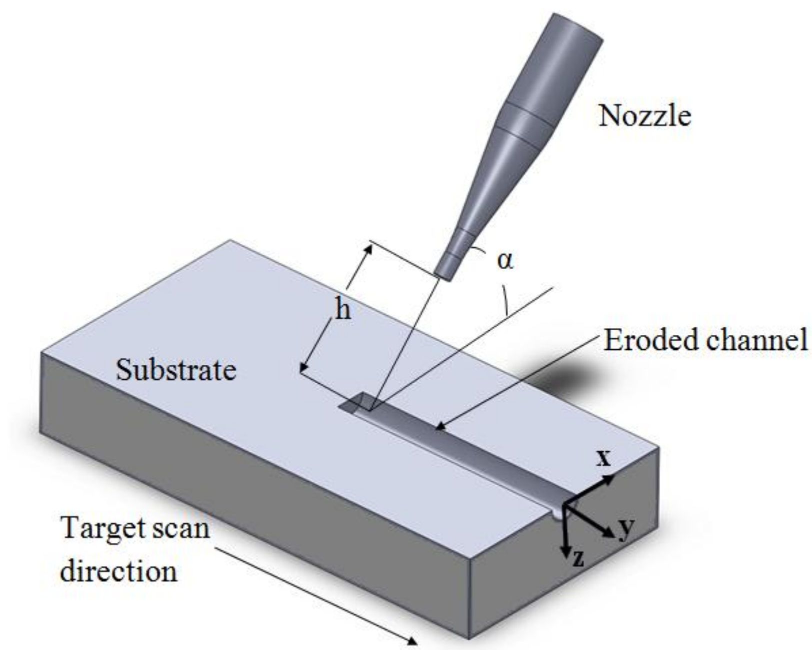

Figure 3-3: Schematic of oblique abrasive jet micro-machining process demonstrating nozzle offset distance *h*, at an angle of incidence *α*, measured in the *x*-*z* plane.

Both the AJM and erosion rate measurements were made on channels machined by moving the stage relative to the fixed nozzle at various speeds. The mass flow rate was measured prior to each experiment by weighing the particles collected after one minute of blasting into a container fitted with filter paper at the entrance to retain the particles while ensuring that there was an insignificant back pressure on the nozzle. The mass flow rate was set sufficiently low (5 - 8 g/min) so that the interference between incoming particles and those rebounding from the surface could be considered negligible, according to the computer model of ref. [29].

3.2 Erosion Rate Measurements

Surface evolution models of AJM require as input the erosion rate (mass of target material removed per unit mass of abrasive used) as a function of the angle of attack, $E(\alpha)$. This is further normalized to $E(\alpha) = E_{90}\, g(\alpha)$, where $g(\alpha)$ is the impact angle dependence of erosion. To determine $g(\alpha)$, erosion experiments were performed by blasting shallow 25 mm long channels into the aluminum 6061-T6 samples at various angles of attack, α, as shown in Figure 3-3.

Channels were machined sufficiently shallow (< 300μm) to ensure that the global impact angle, α, and the local impact angle, θ (refer to Figure 4-1), were effectively the same. The sample scan speed was varied from 0.1-10 mm/s to yield a minimum of five particle doses, while the mass flow rates were kept within the range of 3 - 7 g/min (standard deviation 0.12 g/min) for angles of attack $\alpha = 20°$, 30°, 45°, 60°, and 90° . The particle mass dose per unit length of channel was determined by dividing the mass flow rate by the scan speed. The target mass loss due to blasting was measured using an electronic balance with an accuracy of ± 0.01 mg. The samples were cleaned with compressed air prior to weighing to minimize contamination by deposited particles. The accuracy of the mass loss measurements was verified to be within 3% using an optical profilometer (model ST400, Nanovea, Irvine, CA, USA, Figure 3-4) to determine the channel volume, which was then multiplied by the aluminum alloy density of 2.7 g/mm^3 [41].

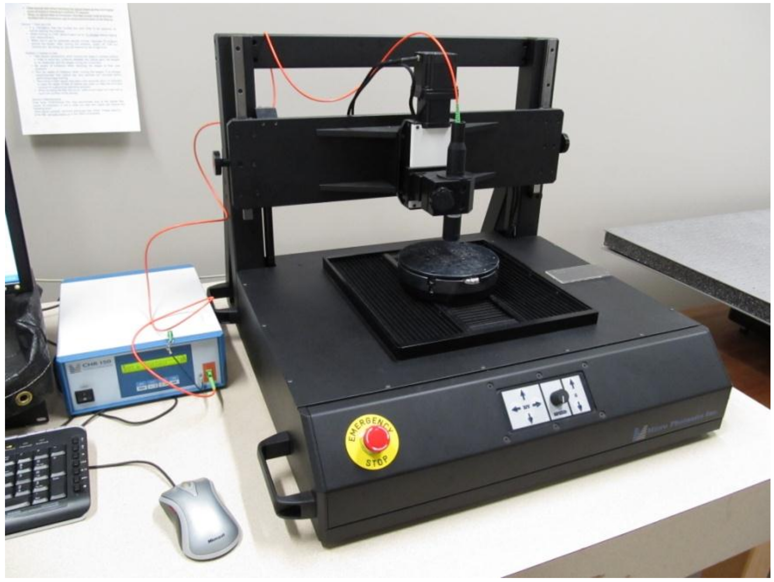

Figure 3-4: The optical profilometer (model ST400, Nanovea, Irvine, CA, USA) used for measuring channel volumes.

For the 316L stainless steel and Ti-6Al-4V alloy specimens, channels were machined at α = 20°, 30°, 45°, 60°, and 90° at flow rates between 5.0-8.0 g/min, with a fixed scan speed of 0.30 mm/s. A stepped channel with 1 cm segments was created corresponding to 1, 3, 5, 7 or 9 passes of the nozzle to achieve a range of doses. Samples were cleaned with compressed air and then measured (minimum of three repeats) using the optical profilometer to determine the channel volume, from which a mass loss value was calculated by multiplying by the densities of 8.0 g/mm^3 and 4.43 g/mm^3 for stainless steel and titanium respectively [33, 34]. The erosion data for all three metals can be found in section 5.1.

The average steady-state erosion rates at each angle for the three tested metals were determined as the slope of the line created by plotting mass loss versus particle dose. The steady state erosion was plotted against angle, and a simple function was used to fit the impact angle dependence, $g(\alpha)$. This relationship is plotted and discussed in section 5.2.

3.3 AJM of unmasked channels in aluminum alloy

In evaluation of the surface evolution model, the procedure used to make unmasked channels of varying depths was similar to that used for the erosion rate tests. Channels were machined in the 6061-T6 aluminum samples at α = 30°, 45°, 60°, and 90° using mass flow rates between 6.0 and 7.6 g/min (standard deviation of 0.12 g/min [9]) and at a fixed scan speed of 0.30 mm/s. A stepped channel was machined with 1 cm segments, each corresponding to 1, 3, 5, 7 or 9 passes of the nozzle under these conditions to achieve a range of depths.

The samples were cleaned with compressed air prior to measurement of the channel profiles using the optical profilometer. Three cross-sectional profiles were measured along each 1 cm length to assess the consistency of the blasting conditions. It was found that these channel depths were always within 10% of the average. A profile for each step was selected for comparison with the surface evolution model for the aluminum alloy. The results of the surface evolution modeling for unmasked channels can be found in chapter 6.

3.4 AJM of masked channels

Masked channels were also machined to evaluate the shape and depth prediction of the surface evolution model. Two 0.3x7.62x1.5 cm hardened steel shims were clamped 200 µm apart on top of the 6061-T6 aluminum, 316L stainless steel, and Ti-6Al-4V alloy substrates to act as masks. This was accomplished by sandwiching a 200 µm feeler gauge in between the two shims, while clamping them laterally, as has been done by previous investigators in the AJM of glass and polymers [9 - 13]. The edges of the sheets were milled square and flat to create a well-defined mask edge and to minimize the amount of under etching that can occur if particles strike the target beneath an overhanging mask edge. The clamping system used is illustrated in Figure 3-5, which was affixed to the computer controlled stage in Figure 3-2. The abrasive jet was aligned with the center of the mask opening at $\alpha = 90°$ (Figure 3-3) with a mass flow rate of 5.0-8.0 g/min (0.12 g/min standard deviation [9]). As with the unmasked channels, a fixed scan rate of 0.30 mm/s was used, and micro-channels were made with 1, 3, 5, 7, and 9 passes of the nozzle. The results of the masked channel prediction by the surface evolution model is presented in chapter 7.

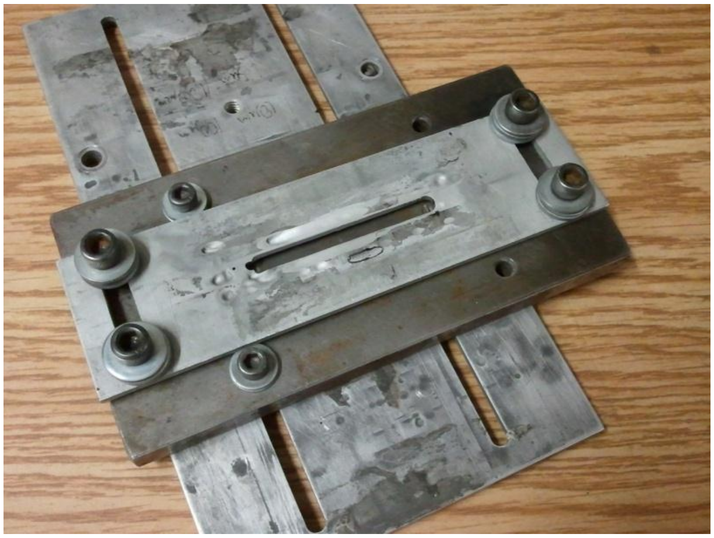

Figure 3-5: The clamping system used to hold the masks to the metal substrate for the AJM of masked channels.

3.5 Velocity Exponent

As mentioned in section 2.3.3, the relationship between velocity and erosion is governed by the velocity exponent, k. The velocity exponent was determined experimentally by measuring the erosion rate at varying pressures between 200 – 600 kPa at normal impact. The pressures are then related to average particle velocities using a free jet model developed by Li et al. [39]. The erosion rate was measured using the method mentioned previously (Section 2.2) for unmasked channels. An erosion rate versus velocity curve was fitted to an exponential equation of the form $E = v^k$, to find the velocity exponent, k for the three metals. Further discussion on the velocity exponent is presented in section 5.4.

Chapter 4: Theory- Surface evolution modeling

In this chapter, a surface evolution model originally developed for the AJM of ductile polymers by Getu et al. [12] will be modified so that it can be used for metals. The model relies on an accurate curve fit of the experimentally determined impact angle dependence of erosion rate. A methodology developed by Oka et al. [18] to fit a trigonometric equation to the erosion data will also be presented.

4.1 Impact angle dependence

Section 2.3.1 highlighted the importance of the impact angle dependence of erosion in ductile materials. For use in the surface evolution model, the present work adopted the form of a dependence suggested by Oka et al. [18]. This relation is governed by Eq. (2-1) and Eq. (2-2).

The first term in Eq. (2-2) accounts for erosion due to plastic deformation induced by the impact energy normal to the surface, while the second factor accounts for the cutting erosion induced by the impact energy parallel to the target surface [12]. In practice, since $n1$ and $n2$ are determined from a best fit to the measured erosion rates at various angles, α, the hardness need not be an accurate value; i.e. any errors or changes in the actual Hv due to strain hardening will simply be compensated in Eq. (2-2) by the best fit values of $n1$ and $n2$.

The experimentally determined $g(\alpha)$ data were fitted to Eq. (2-2) to determine $n1$ and $n2$ using the non-linear least squares method. Since the hardness was also a fitted parameter and was unknown under dynamic impact conditions, nominal hardness values of 0.828 GPa, 0.870 GPa, and 2.370 GPa were assumed for 6061-T6, 316L and Ti-6Al-4V alloys, respectively, based on three times the yield strength [44].

4.2 Surface evolution model

As will be shown in Section 5.1, all three metals eroded in a typical ductile fashion. The time-dependent surface evolution of the etched cross-sectional channel profile for these metals could thus be modeled using the approach developed by Getu et al. [12, 13] for ductile polymer targets. This was based on the pioneering models originally developed by ten Thije Boonkkamp and Jansen [45], and Slikkerveer et al. [46] for the AJM of brittle materials.

The two-dimensional surface evolution equation that accounts for the dependence of erosion rate on the local impact angle, θ, for ductile erosion is [12]:

$$z_{,t} = \left(\frac{1}{\rho_s} C\, V(x)^k \Phi(x)\right)\left(\sqrt{1+z_{,x}^2}\right) g(\theta) \tag{4-1}$$

where ρ_s is the density of the target material (kg/m^3), $\Phi(x)$ is the particle mass flux (kg·m^{-2}·s^{-1}), $V(x)$ is the particle velocity distribution at the surface (m/s), k is the velocity exponent, and C is a constant. $z_{,t}$ and $z_{,x}$ are the partial derivatives of the profile depth, z, with respect to time, t, and location x, respectively (Figure 4-1a). The local impact angle θ is measured between the local tangent to the surface and the incident velocity vector (Figure 4-1b), and for globally normal incidence (α = 90°), it is equal to [12]:

$$\theta = \left(\frac{\pi}{2} - \arccos\left(\frac{1}{\sqrt{1+z_{,x}^2}}\right)\right)$$

(4-2)

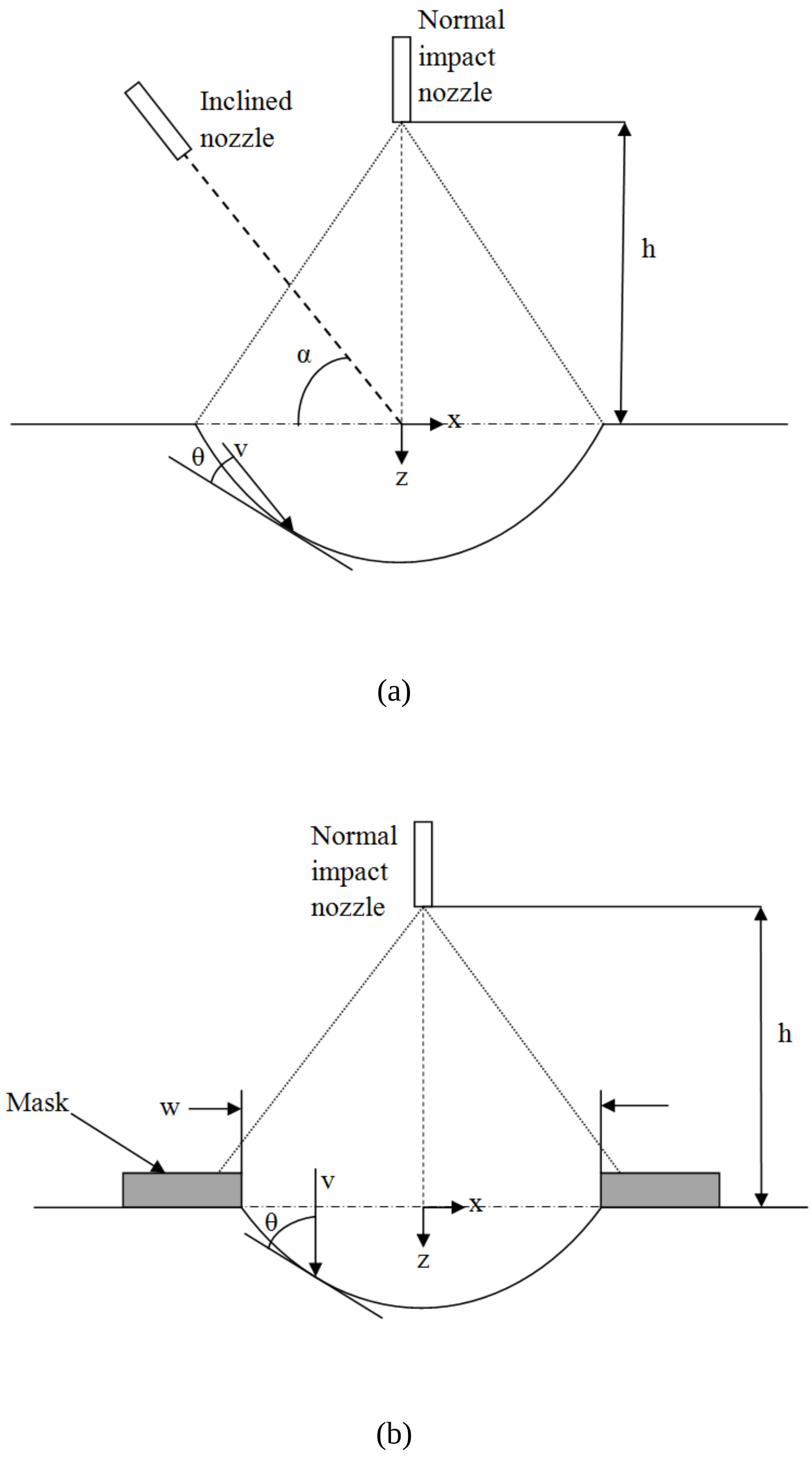

Figure 4-1: Coordinate system and geometry used for surface evolution prediction for (a) unmasked erosion, and (b) masked erosion. θ is the local angle of the incident velocity vector, v, and α is the global angle of attack measured in the x-z plane.

4.3 Application to Unmasked Channels

The potential of the abrasive jet to erode, the so-called 'erosive efficacy', *Q(x)*, is given by the first bracketed term of Eq. (4-1). Since the particle flux, Φ, and velocity, *V*, for the conditions utilized in the present tests were not known, *Q(x)* was inferred by curve fitting a measured shallow (z_x~0) profile, as was suggested in ref. [12]. Based on previous measurements of particle flux and velocity for typical AJM blasting systems [9], the non-dimensional form of *Q(x)* that was used to fit the first-pass profile data points was given by:

$$Q(x)_{normal} = c\left(e^{-(bx)^2}\right)(1 - a|x|)^k \tag{4-3}$$

where *k* is the velocity exponent, and *a*, *b* and *c* are the fitted first-pass parameters. Eq. (4-3) can also be modified using a simple coordinate transformation (Figure 4-2) similar to that adopted in [10], and used to fit the non-dimensional first-pass profile for unmasked channels machined at oblique angles of attack ($\alpha \leq 90°$, Figure 4-2):

$$Q(x)_{Oblique} = \frac{c}{(h \pm x\cos(\alpha))^2}\left(e^{-\left(\frac{bx\sin(\alpha)}{h \pm x\cos(\alpha)}\right)^2}\right)\left(1 - a\,\frac{|x|\sin(\alpha)}{h \pm x\cos(\alpha)}\right)^k \tag{4-4}$$

where the ± in Eq. (4-4) indicates that a positive sign should be used when the global angle of attack, α, is measured from the -*x* axis, and a negative sign when α is measured from the +*x* axis.

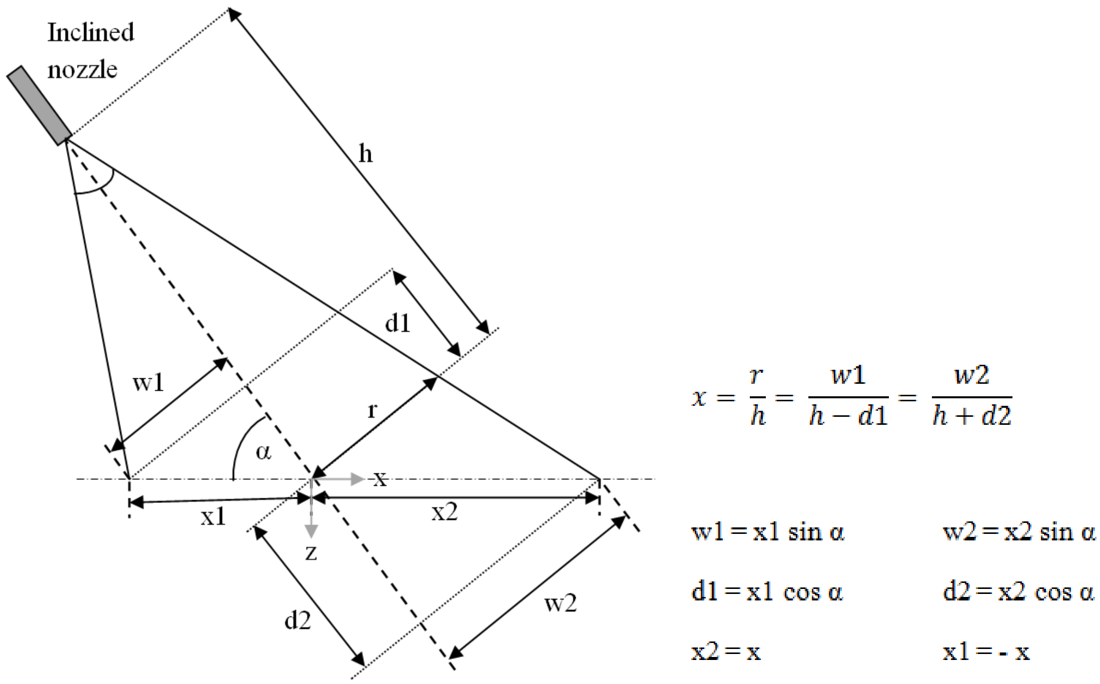

Figure 4-2: Coordinate transformation used in Eq. (4-4) for oblique erosive efficacy.

For oblique incidence, the relationship between the global and local impact angles (Figure 4-1a) is,

$$\theta = \left(\frac{\pi}{2} - \arccos\left(\frac{\cos\alpha + z_{,x}\sin\alpha}{\sqrt{1+z_{,x}^2}}\right)\right) \tag{4-5}$$

4.4 Application to Masked Channels

Equation (4-1) can also be used to predict surface evolution in masked AJM [3, 4] if the disturbance in the incident flux by the mask edges can be determined. The erosive efficacy, *Q(x)*, which includes these mask edge effects can be found experimentally by solving Eq. (4-1) for the erosive efficacy (the first bracketed term) using an experimentally determined profile *z(x, t)*, as described in [9]. Briefly, Eq. (4-1) and Eq. (4-3) can be rearranged to solve for the erosive efficacy *Q(x)* for masked channels as follows [9]:

$$Q(x)_{masked} = \frac{z_{,t}}{\left(\sqrt{1+z_{,x}^2}\right)g(\theta)} \tag{4-6}$$

with

$$(z_{,t})_i = \frac{z(x_i,\ t) - z(x_i,\ 0)}{t}$$

$$(z_{,x})_i = \frac{z(x_{i+1},t) - z(x_i,t)}{x_{i+1} - x_i} \tag{4-7}$$

where x_i and z_i are data points on the experimental profile. Eq. (4-7) is a first order approximation to the time and space derivatives in Eq. (4-6). A polynomial or exponential equation is fitted to the erosive efficacy in Eq. (4-6), which can then be used in Eq. (4-1) to solve the surface evolution equation.

Chapter 5: Fundamental Erosion Behavior of Metals

The collected erosion data was used to derive the impact angle dependence by taking the average erosion rate as the slope of the volumetric loss versus dosage graph for each impact angle. The relation was then modeled by the trigonometric equation presented by Oka et al. [18] for use in the surface evolution model. This chapter presents the erosion data, impact angle dependence and comments on the differences in the erosion rates between the aluminum, stainless steel and titanium alloys and the significance of particle embedding.

5.1 Measured erosion rates

Figure 5-1 shows the plot of volumetric erosion loss versus dose for aluminum 6061-T6, Ti-6Al-4V alloy, and 316L stainless steel machined at 90°. No incubation period was noted since all three lines pass through the origin. The results indicate that aluminum has a higher volumetric erosion rate, E_v, (0.30 mm^3/g; slope of line) than titanium alloy (0.147 mm^3/g), which has a higher erosion rate than stainless steel (0.106 mm^3/g), on a volumetric basis. In contrast, it is noted that the mass-loss erosion rates for the three metals were quite similar owing to the significant density differences in the metals.

The volumetric erosion rates of these metals as determined from Fig 5-1correlated with the elastic modulus (E) and fracture toughness (K_{IC}), as shown in Table 5-1. The combination of these two properties yield the strain energy release rate, in the form of K_{IC}^2/E, which is the energy required to produce a unit crack extension. From Table 5-1, it is concluded that the strain energy release rate is inversely proportional to the erosion rate. O'Flynn et al. [26] found a similar relation between the erosion rate and product of toughness (deformation energy per unit volume of material removed required to produce fracture) and uniform strain (amount of strain required to cause the material to neck during a tensile test).

In addition, it has been noted that there is a tendency for titanium to absorb oxygen, hydrogen and nitrogen, which may induce embrittlement [22]. Titanium is also known to be more notch sensitive than steels [42]. All of these may have contributed to the higher erosion rate.

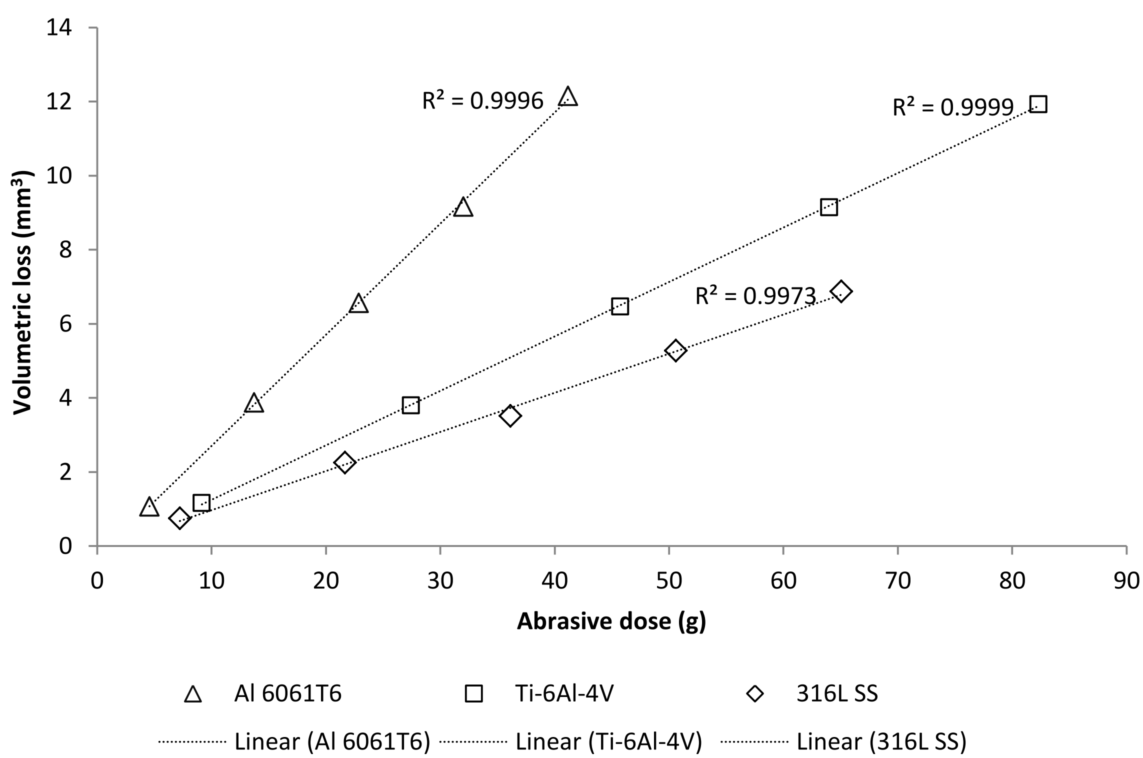

Figure 5-1: Volumetric loss vs. dose for the erosion of aluminum 6061-T6, 316L stainless steel, and Ti-6Al-4V alloy by an abrasive jet at 90° impact angle. The error in repeated measurements was less than 1%.

Table 5-1: Properties correlating with erosion rate, sourced from [41-43, 50].

Property	Aluminum 6061 T6	Ti-6Al-4V alloy	316L Stainless steel
Fracture toughness (MPa$\sqrt{m}$)	29.7	47	250
Elastic modulus (GPa)	68.9	105	193
Strain energy release rate (J/m^2)	0.0128	0.0210	0.3238

Harsha and Bhaskar [23] conducted erosion tests on several metals and also could not find any relationship between the nominal low strain-rate material properties (such as yield and tensile strength, elastic modulus, and ductility) and their erosion rates. As in the present case, they found that the aluminum and stainless steel had quite similar mass loss erosion behavior. Rodriguez et al. [28], Sapate and Rama Rao [29] and Oka et al. [18] all concluded that material hardness generally correlates inversely with the erosion resistance when testing metals of varying hardness. However, this was not noted in this study.

It was thought that 316L stainless steel may have resulted in a lower erosion rate due to an increase in surface hardness by strain hardening. To investigate this, a sample machined at 45° was electrochemically polished using an electro-polisher (ELECTROMET® 4 Polisher/Etcher, Buehler, Whitby, Ontario) with a combination of 50% sulfuric acid (96% purity) and 50% orthophosphoric (85% purity) at 75°C for 180 s to remove surface waviness. The Vickers hardness was then measured inside and outside the channel (minimum 4 repeats) and only a 4.6 % increase in surface hardness was measured.

An attempt was made to investigate the effects of cryogenic temperatures on unmasked channels in 316L stainless steel. The motivation was that an increase in erosion rate would be observed due to the embrittlement of the steel at lower temperatures, hence a faster material removal during a machining operation. The effects of cryogenic temperatures on abrasive jet micro-machining of 316L stainless steel is presented in Appendix A.

5.2 Impact Angle Dependence

The measured erosion rates as a function of the impact angle based on the mass loss measurements are shown in Figure 5-2 for the three metals. Figure 5-3 show the same data, but plotted on the basis of volumetric erosion. The figures also shows the best fits to Eq. (2-1) using Eq. (2-2) and a non-linear least squares curve fit (MATLAB version 7.8.0.347, curve fitting tool box, Mathworks, Natick, MA, USA). The best fit to the exponents *n1* and *n2* and the *Hv* values are summarized in Table 5-2.

The maximum erosion rate for the metals occurs between α = 20° and 35°, similar to the findings of Oka et al. [18] for ductile metals blasted with 325 µm silica sand particles. In the case of the aluminum alloy, the maximum erosion rate, 1.2 mg/g, was similar to that reported by Neilson and Gilchrist [20], who used larger aluminum oxide particles and several velocities to obtain maximum erosion rates ranging from 0.6 to 3.0 mg/g. It was also within the range measured by Veerabhadra Rao et al. [17]; i.e. 0.42 - 1.1 mg/g using 30 µm crushed glass. Singh et al. [24] reported erosion rates in the range of 0.6 mg/g at 90° to 1.2 mg/g at 30°, where the maximum erosion was observed for 316 steel when eroded by 160 µm SiC particles at 129 m/s. This compares well with the present measurements, which were in the range of 0.8-1.5 mg/g (Figure 5-2). Morrison and Scattergood [25] found the erosion rate of 304 stainless steel to be in a similar range, between 0.4 and 1.0 mg/g, using 37-270 µm alumina abrasive particles at 100 m/s.

Emiliani and Brown [21] obtained an erosion rate of 0.08 mg/g at 90° when eroding Ti-6Al-4V alloy with 210 µm silica spherical particles at a velocity of 61 m/s. A maximum erosion rate of 0.13 mg/g was found at 30° by Yerramareddy and Bahadur [22], who eroded Ti-6Al-4V alloy aged at 940°C with 10-150 µm SiC particles at 55 m/s. In the present case, a faster 106 m/s particle velocity was used to attain a maximum erosion rate of 1.25 mg/g at 20°.

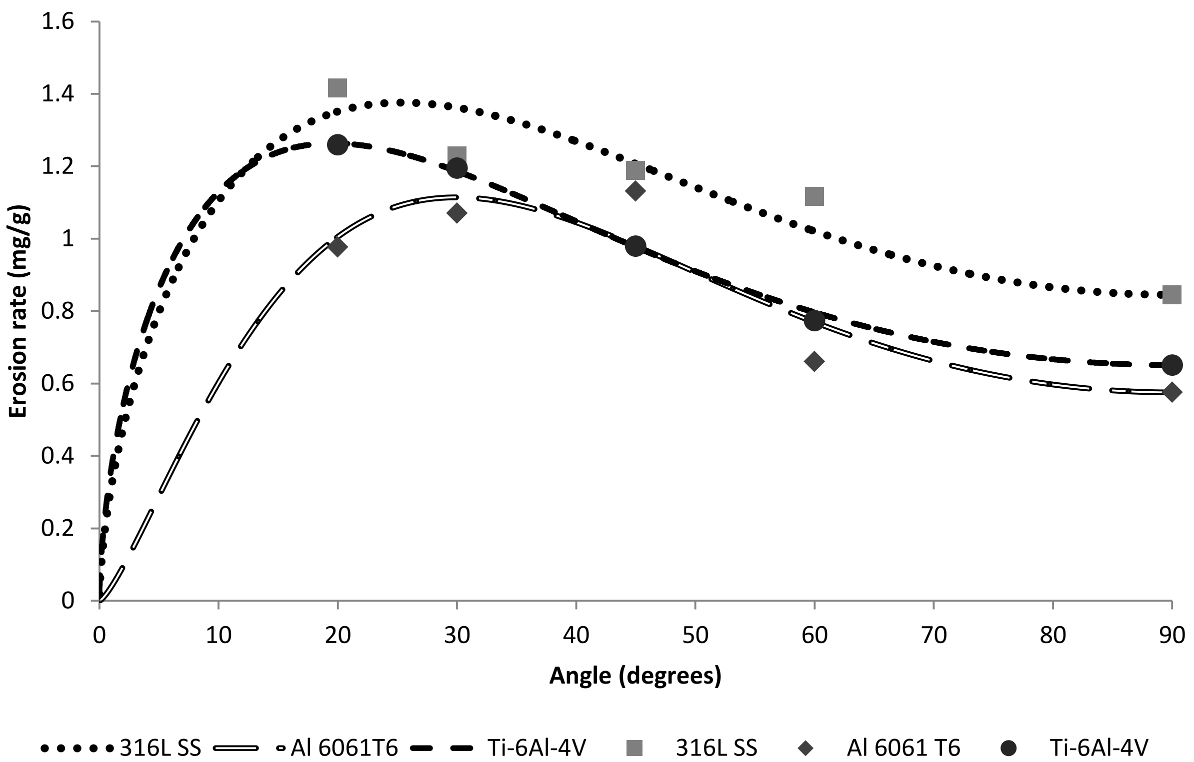

Figure 5-2: Erosion rate of 6061-T6 aluminum, Ti-6Al-4V alloy and 316L stainless steel by 50 μm aluminum oxide particles at a velocity of 106 m/s as a function of angle of attack. Symbols indicate measured values based on average mass loss, dashed lines are best fits to Eq. (2-1) using Eq. (2-2).

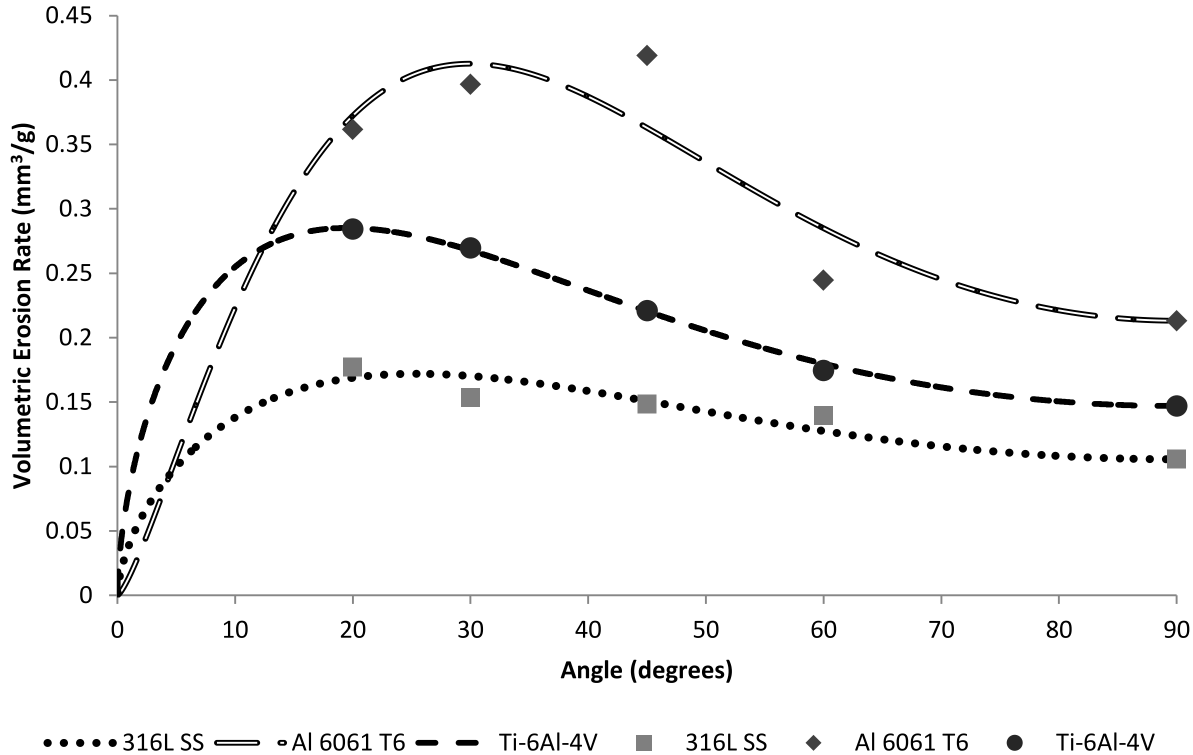

Figure 5-3: Volumetric erosion rate as a function of angle of attack for the three metals.

Table 5-2: Best-fit parameters of Eq. (2-2) for the impact angle dependence of erosion (Figure 5-2).

Parameter from Eq.(2-2)	*n1*	*n2*	*Hv*
Aluminum 6061-T6	1.340	4.590	0.828
316L Stainless steel	1.981	5.677	0.870
Ti-6Al-4V alloy	0.140	0.872	2.370

Figure 5-4 shows scanning electron micrographs of single impact sites taken at the periphery of the blast zones on the metal surfaces. Evidence of particle cutting and ploughing with associated pile-up at the edges of the crater signifies ductile erosion.

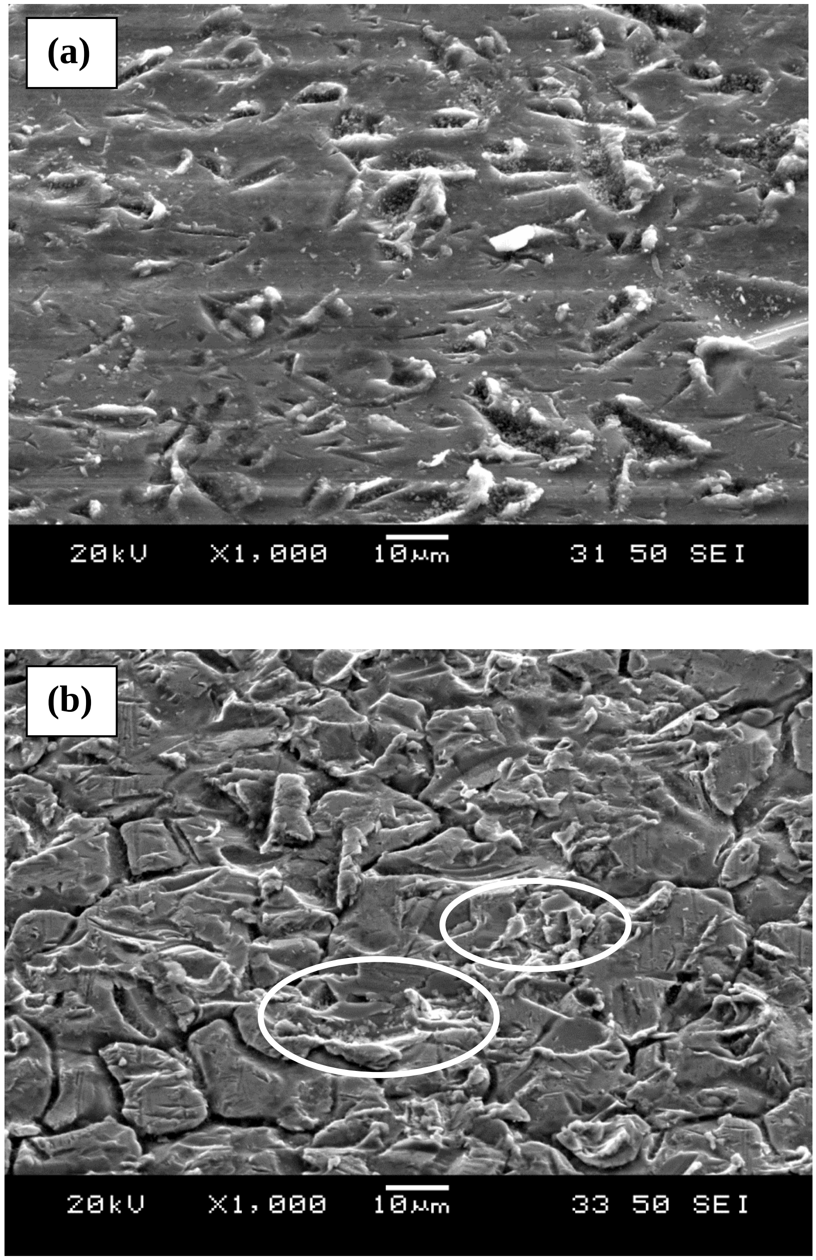
(a)
20kV X1,000 10µm 31 50 SEI
(b)
20kV X1,000 10µm 33 50 SEI

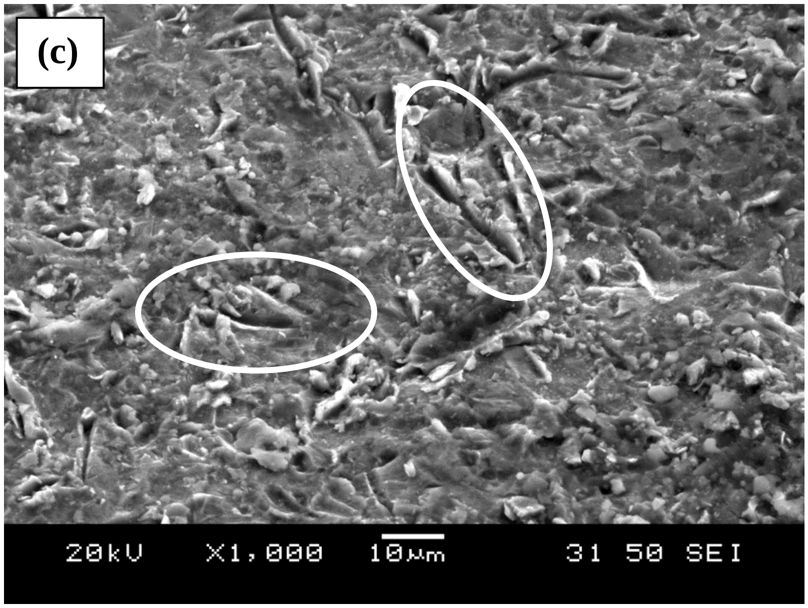

Figure 5-4: SEM images (tilted at 40°) of single impact sites in (a) aluminum 6061-T6, (b) 316L stainless steel, and (c) Ti-6Al-4V alloy at impact angles of 45° and velocity of 106 m/s. Particles were moving from left to right.

The roughness of the three metals was also measured as a function of dose to investigate if it may have had an effect on the relative erosion rates observed in Figure 5-1. Appendix C presents the roughness versus dose graphs for unmasked channels at normal impact.

5.3 Particle embedding

While Neilson and Gilchrist [20] and Veerabhadra Rao et al. [17] noted a distinct incubation period where aluminum samples initially gained weight due to embedding particles, this phenomenon was not observed in the present study. However, some evidence of embedded particles was obtained using a particle tagging technique as shown in Figure 5-5. Detailed procedures of other techniques tried in this thesis can be found in Appendix B. In this case, an unmasked channel was blasted with ink coated particles and examined with an optical microscope. The amount of embedding was relatively small, being on average only about one embedded particle for every 3 mm^2.

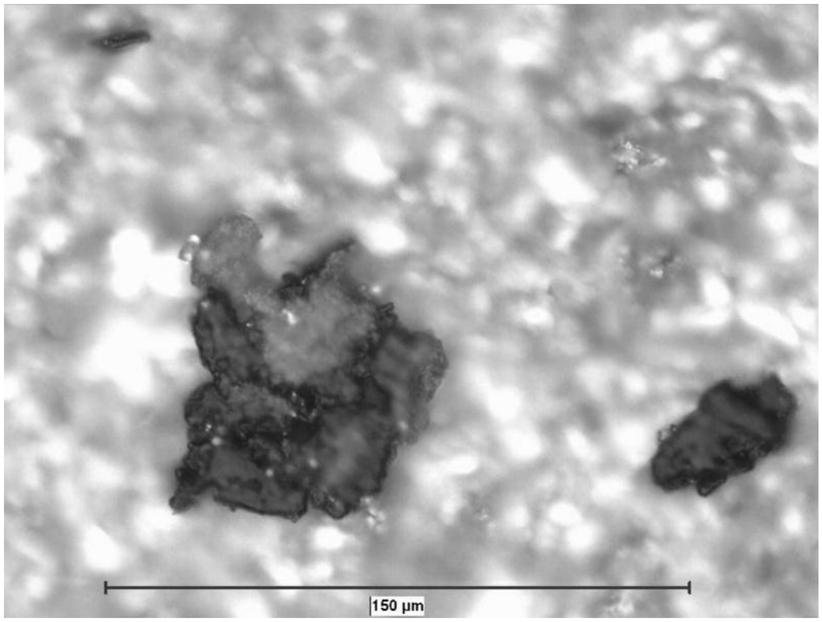

Figure 5-5: Ink coated aluminum oxide particles embedded in 6061-T6 after abrasive jet micro-machining (500x magnification).

Examination of a masked channel with a scanning electron microscope (Figure 5-6) revealed possible evidence of embedded particles within the channel, however the particles were widely distributed, and difficult to quantify. Energy-dispersive x-ray (EDX) detection showed that the particles shown in Figure 5-6 contained a high fraction of aluminum, although it was not possible to conclusively identify them as aluminum oxide.

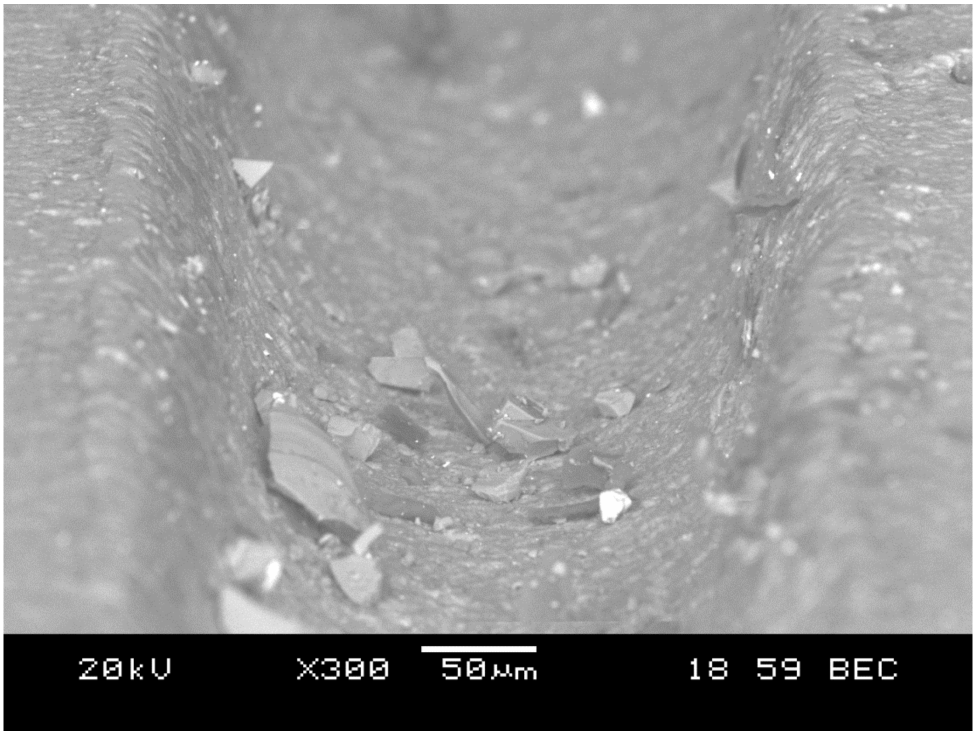

Figure 5-6: An S.E.M. image of embedded particles in a masked channel in aluminum 6061-T6 alloy after being machined with 50 µm aluminum oxide particles (300x magnifications).

Scanning electron micrographs and EDX analysis of the eroded surfaces of 316L stainless steel showed a significant amount of particle embedding, with a lesser amount in the Ti-6Al-4V alloy (Figure 5-7). Mapping the EDX aluminum distribution gave a 30% surface coverage of aluminum particles in stainless steel, and only 5% in the much harder titanium. The higher particle embedding observed in stainless steel could contribute to its lower erosion rate due to a layer of erodent protecting the surface from further erosion.

Most previous studies of metal erosion reported little evidence of particle embedding. Morrison and Scattergood [25] did not find any evidence suggesting particle embedding when eroding 304 stainless steel with varying sizes of aluminum oxide abrasive. No evidence of particle embedding was found by Yerramareddy and Bahadur [22] when SiC erodent was used on Ti-6Al-4V alloy. However, Emiliani and Brown [21] noted the entire surface of Ti-6Al-4V alloy eroded by 210µm spherical glass particles was coated with a "glassy layer", which was said to be caused by the glass melting and embedding upon impact due to heat. Harsha and Bhaskar

[23] eroded aluminum, brass, copper, mild steel, stainless steel and cast iron using 150 – 300μm silica sand, and noted sand particles remaining on the surfaces.

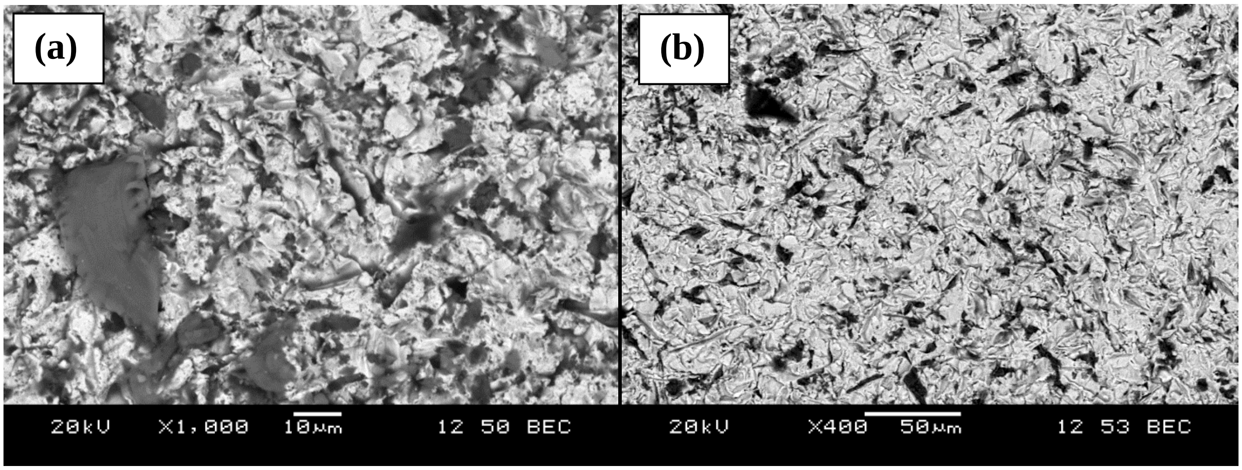

Figure 5-7: SEM images of embedded aluminum oxide particles (darker spots) in (a) 316L stainless steel and (b) Ti-6Al-4V alloy.

5.4 Velocity Exponent

The velocity exponent was determined experimentally by measuring the erosion rate at varying pressures, which were related to average particle velocities using the free jet model developed by Li et al. [39]. An erosion rate versus velocity curve was fitted to an exponential equation of the form $E = v^{k}$, to find the velocity exponent, k. These graphs can be found in Appendix D.

A value of k = 3.44 was obtained for 6061-T6 aluminum, which compares well to k=3 found by Sheldon et al. [39] and k=3.68 reported by Veerabhadra Rao et al. [17]. Values of k = 2.21 and k = 2.04 were found for 316L stainless steel and Ti-6Al-4V alloy, respectively. These compare well with the results of by Singh et al. [24] (2.2 – 2.7) for stainless steels, and Yerramareddy and Bahadur [22] (2.35) for Ti-6Al-4V alloy.

Chapter 6: Surface evolution of unmasked channels in 6061-T6 aluminum

In Chapter 5, the collected erosion data yielded a trigonometric relationship, Eq. (2-2) that accurately fit the angular impact dependence of erosion for the three metals. In this chapter, this relationship will be used in the surface evolution equation, Eq. (4-1), to predict the cross sectional profiles of the unmasked channels described in section 4.2 and 4.3 that were machined at normal impact in aluminum 6061-T6.

6.1 Normal incidence

The predicted channel profiles were obtained using Eq. (4-3), determined from the best-fit to a shallow channel machined at normal incidence, together with the initial condition that $z(x,0) = 0$. Eq. (4-1) was solved using the method of lines implemented in Mathcad 11 (Mathsoft Engineering & Education, Inc, Cambridge, MA. USA) with 300 time and space steps. This yielded the channel profile predictions shown in Figure 6-1.

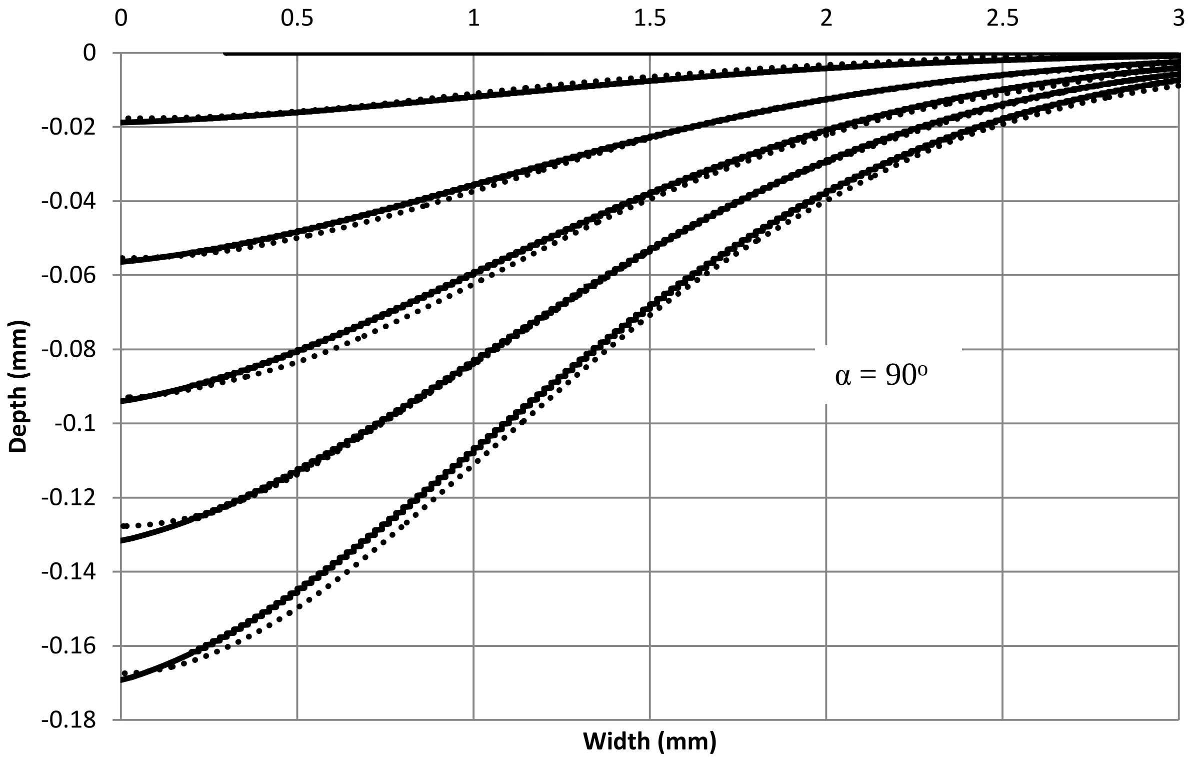

Figure 6-1: Measured (dots) and predicted (solid lines; Eq. (4-1)) channel profiles for unmasked erosion in 6061-T6 aluminum at α=90° at a velocity of 106 m/s. Half the symmetric profiles are shown for 1, 3, 5, 7 and 9 passes. The third pass was used to fit Eq. (4-4) which yielded non-dimensional values of *a*, *b* and *c* of 0.9729, 10.74, and -1.14, respectively.

The predicted unmasked channel profiles matched the measured cross-section shapes quite accurately for all passes of the jet.

6.2 Oblique incidence

The surface evolution model of Eq. (4-1) was used by Getu et al. [13] to predict the symmetric channel profiles resulting from abrasive jet machining of polymers with the nozzle inclined in the same plane as the target scan direction; i.e. the *y-z* plane of Figure 3-3. However, the present work was the first time Eq. (4-1) has been used to predict the asymmetric cross-sectional shape of a channel machined with the nozzle inclined in the plane perpendicular to the scan direction (Figure 3-3). In this case, the shallow first or third-pass profile was fitted to the erosive efficacy expression of Eq. (4-4), and then Eq. (4-1) was solved with the boundary conditions $z(x, 0) = 0$, for $\alpha = 30°$, 45°, and 60°. The results are plotted in Figures 6-2 – 6-4.

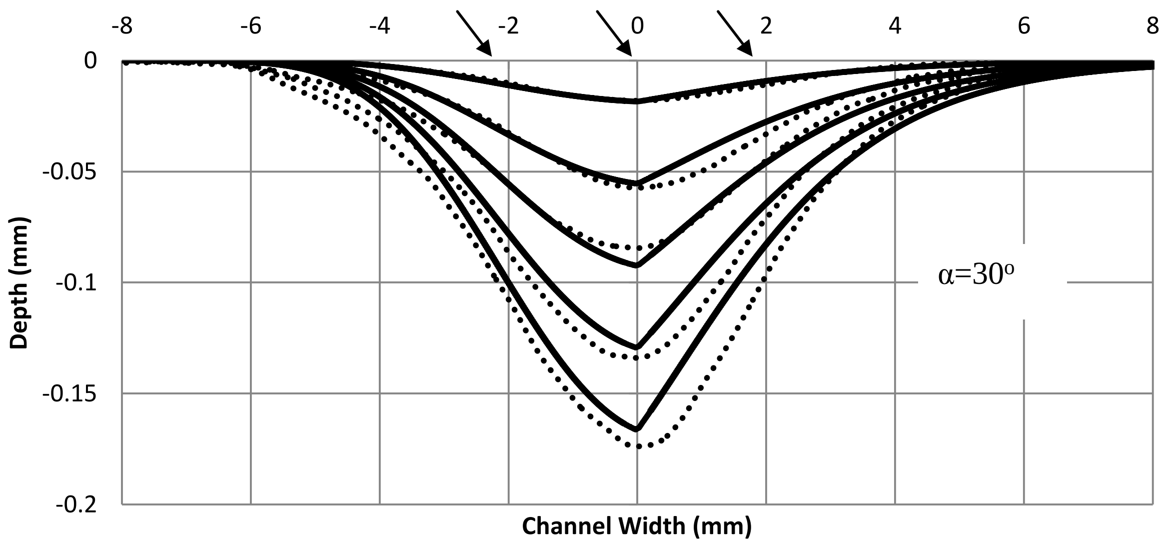

Figure 6-2: Comparison of the unmasked measured profiles (dots) and the predicted profiles (solid lines) in 6061-T6 aluminum at α = 30° and at a velocity of 106 m/s (particle incident trajectories indicated by arrows) for 1, 3, 5, 7 and 9 passes. Note the 1:100 axis scale greatly distorts the apparent aspect ratio. The shallow channel fit to Eq. (4-4) was based on the third pass and yielded non-dimensional values of 1.831, 10.41 and –1.062 for a, b and c respectively.

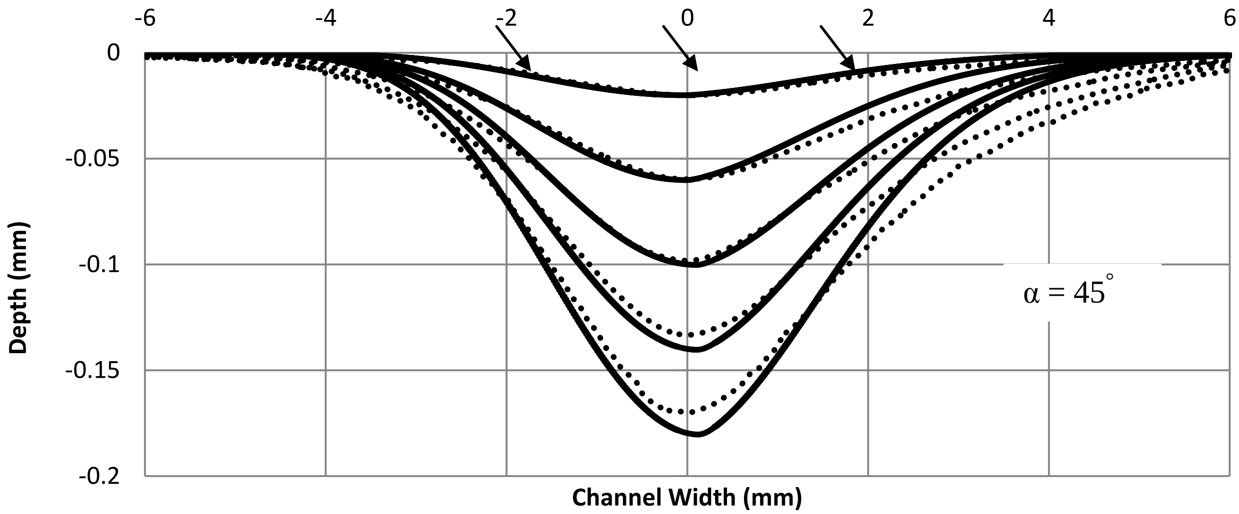

Figure 6-3: Comparison of the unmasked measured profiles (dots) and the predicted profiles (solid lines) in 6061-T6 aluminum at $\alpha = 45°$ and at a velocity of 106 m/s (particle incident trajectories indicated by arrows) for 1, 3, 5, 7 and 9 passes. Note the 1:100 axis scale greatly distorts the apparent aspect ratio. The shallow channel fit to Eq. (4-4) was based on the third pass and yielded non-dimensional values of 0.5, 12 and -1.249 for *a*, *b* and *c*, respectively.

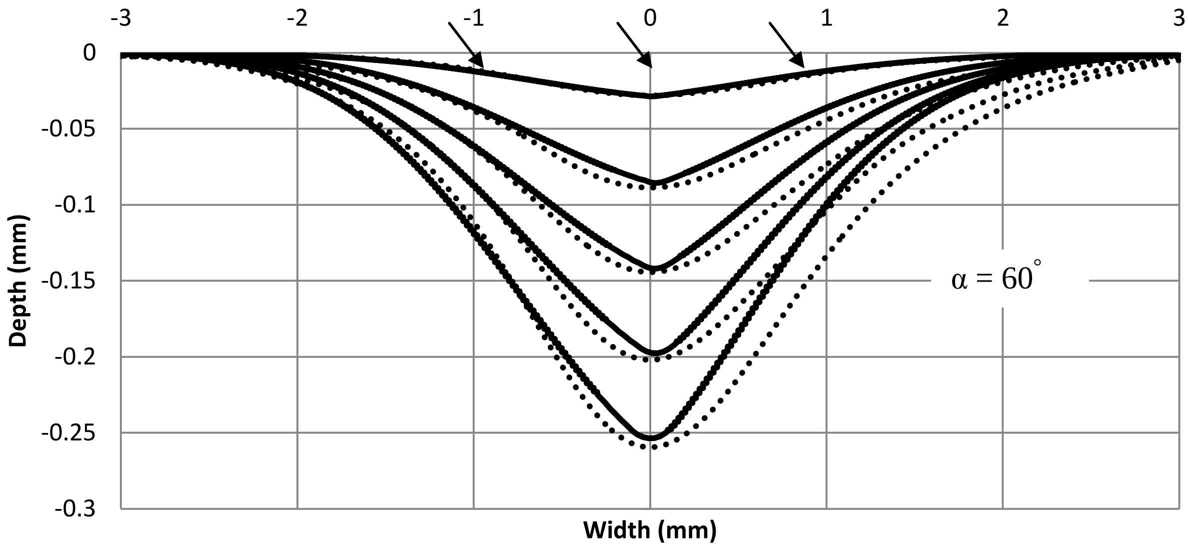

Figure 6-4: Comparison of the unmasked measured profiles (dots) and the predicted profiles (solid lines) in 6061-T6 aluminum at α = 60° and at a velocity of 106 m/s (particle incident trajectories indicated by arrows) for 1, 3, 5, 7 and 9 passes. Note the 1:100 axis scale greatly distorts the apparent aspect ratio. The shallow channel fit to Eq. (4-4) was based on the first pass and yielded non-dimensional values of 2.72, 15.34, and -0.5978 for *a*, *b* and *c* respectively.

Figures 6-2 – 6-4 show the predicted and measured cross-sections of asymmetric unmasked channels in 6061-T6 aluminum for impact angles of 30°, 45°, and 60°, respectively. All three figures indicate that, on average, the model predictions of both the shape and depth are quite good, with a maximum error in the center depth of approximately 4%. There is some under-prediction of the channel width on the right side of the oblique impact profiles.

Chapter 7: Surface evolution of masked channels

In Chapter 6, Eq. (4-1) was solved for unmasked channels using Eq. (4-3) and Eq. (4-4) as the erosive efficacy for channels at normal and oblique impact machined in aluminum. In this chapter, Eq. (4-1) will be used with a modified erosive efficacy presented in section 4.4, to predict the evolution of masked channels in aluminum, stainless steel and titanium alloys.

7.1 Masked AJM model prediction

An SEM image of the masked channel in the aluminum alloy is shown in Figure 7-1. The measured profiles of the masked channels that were machined with $\alpha = 90°$ are shown in Figures 7-2 – 7-4 for the three metals. They exhibited relatively flat bottoms, notably in the first and third passes, similar to what was found by Getu et al. for the AJM of polymers [13]. Minimal mask under-etching was observed for shallow passes, while slight under-etching was noted in deeper channels.

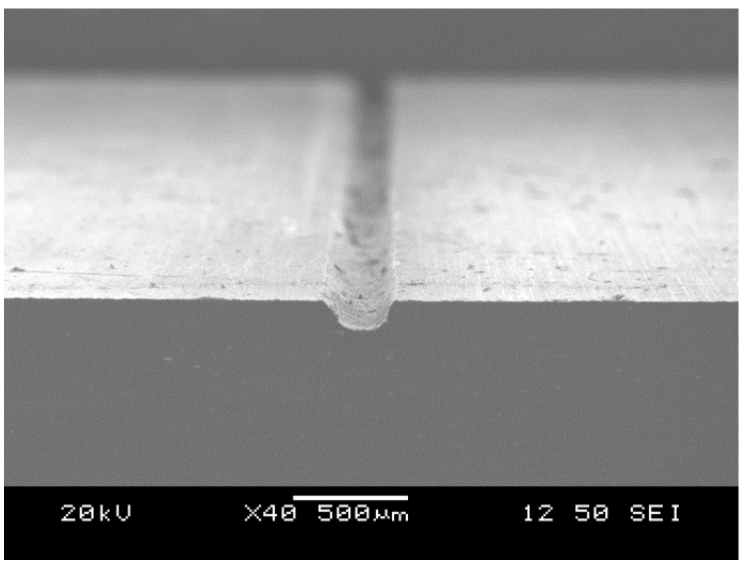

Figure 7-1: Scanning electron microscope image of a masked channel in aluminum 6061-T6 after five passes of the jet at a scan speed of 0.3 mm/s and a particle velocity of 106 m/s.

It was demonstrated in previous work that a best fit of the first-pass profile can be used to represent the erosive efficacy through the mask opening that accounts for the disturbance created by particle-to-mask impact and ricochet [12, 13]. In an earlier work, a sixth-order polynomial provided a good fit to the first-pass profile as an approximation for the erosive efficacy, *Q(x)*, for the AJM of polymers. In the present case, a first-order approximation was used to iteratively determine the erosive efficacy (Eq. (4-6)) using an experimentally determined third-pass profile for the aluminum and titanium substrates, similar to the approach of Ghobeity et al. [9]. In the case of stainless steel, a third pass profile in the form of an exponential function was found to better fit the erosive efficacy for use in the surface evolution model.

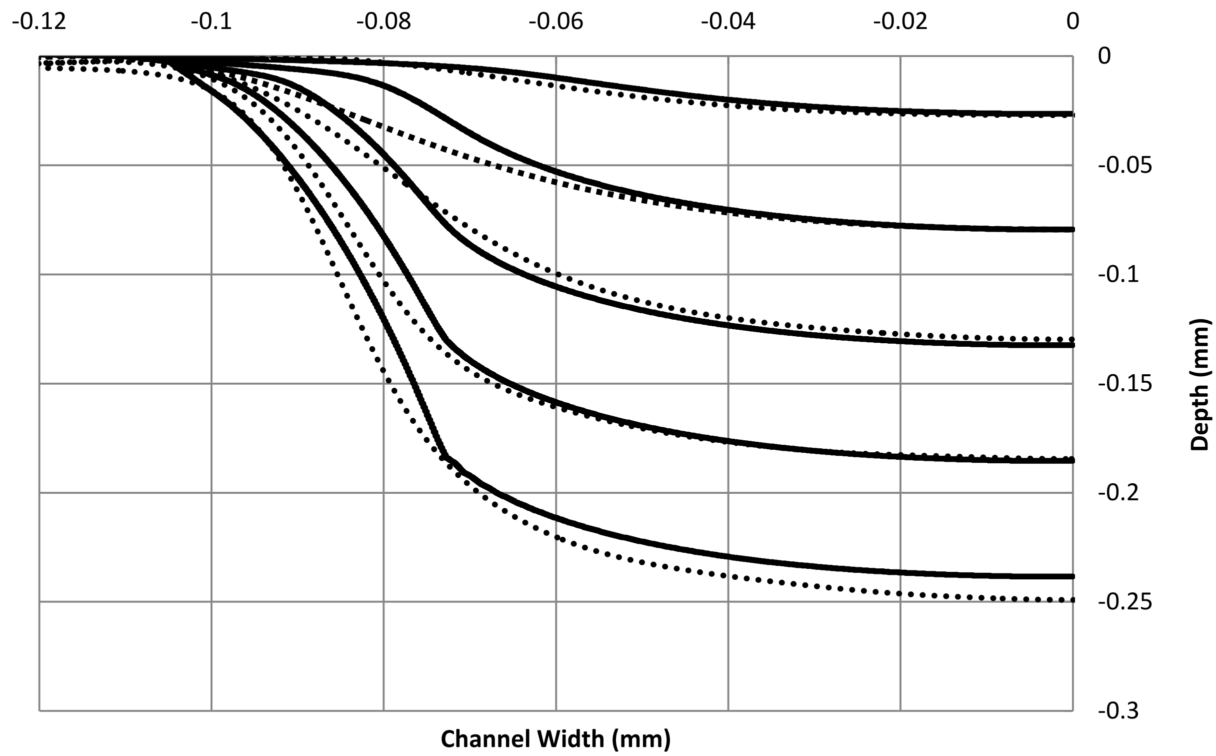

Figure 7-2: Comparison of the predicted (solid lines) and measured (dots) profiles of masked channels in aluminum 6061-T6 at $\alpha = 90°$ for 1, 3, 5, 7 and 9 passes. One half of a symmetric channel is shown. The mask edge was located at x = -0.1. The third-pass experimental profile yielded a curve fit erosive efficacy using the method of (Eq. (4-6)) of $Q(x) = 1.255\text{x}10^4\, x^9 + 4.161\text{x}10^4\, x^8 + 5.681\text{x}10^4\, x^7 + 4.068\text{x}10^4\, x^6 + 1.642\text{x}10^4\, x^5 + 3.581\text{x}10^3\, x^4 + 396.266\, x^3 + 28.785\, x^2 + 0.558\, x - 0.997$.

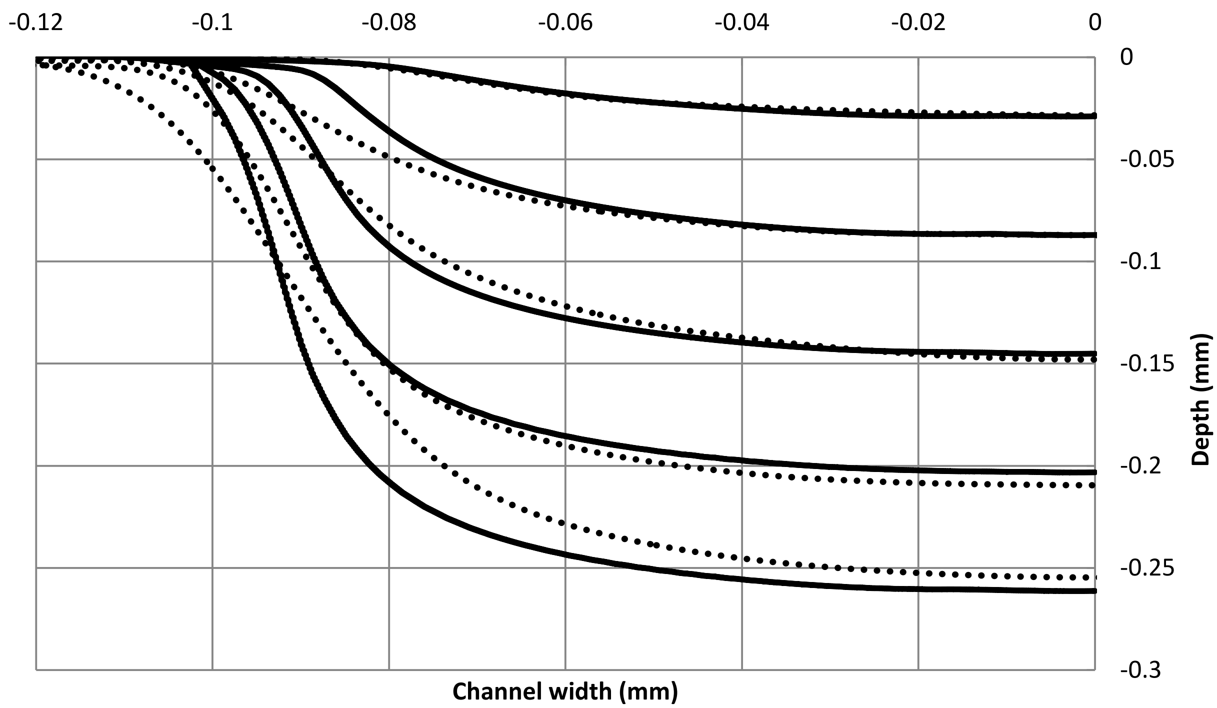

Figure 7-3: Comparison of the predicted (solid lines) and measured (dots) profiles of masked channels in Ti-6Al-4V alloy at α = 90° for 1, 3, 5, 7 and 9 passes. One half of a symmetric channel is shown. The mask edge was located at x = -0.1. The third-pass experimental profile yielded an erosive efficacy (Eq. (4-6)) of $Q(x) = -4.275\text{x}10^6\, x^{12} - 1.308\text{x}10^7\, x^{11} - 1.613\text{x}10^7\, x^{10} - 9.616\text{x}10^6\, x^9 - 2.031\text{x}10^6\, x^8 + 8.261\text{x}10^5\, x^7 + 6.888\text{x}10^5\, x^6 + 2.077\text{x}10^5\, x^5 + 3.297\ \text{x}10^4\, x^4 + 2.755\text{x}10^3\, x^3 + 110.264\, x^2 + 1.589\, x - 0.994$.

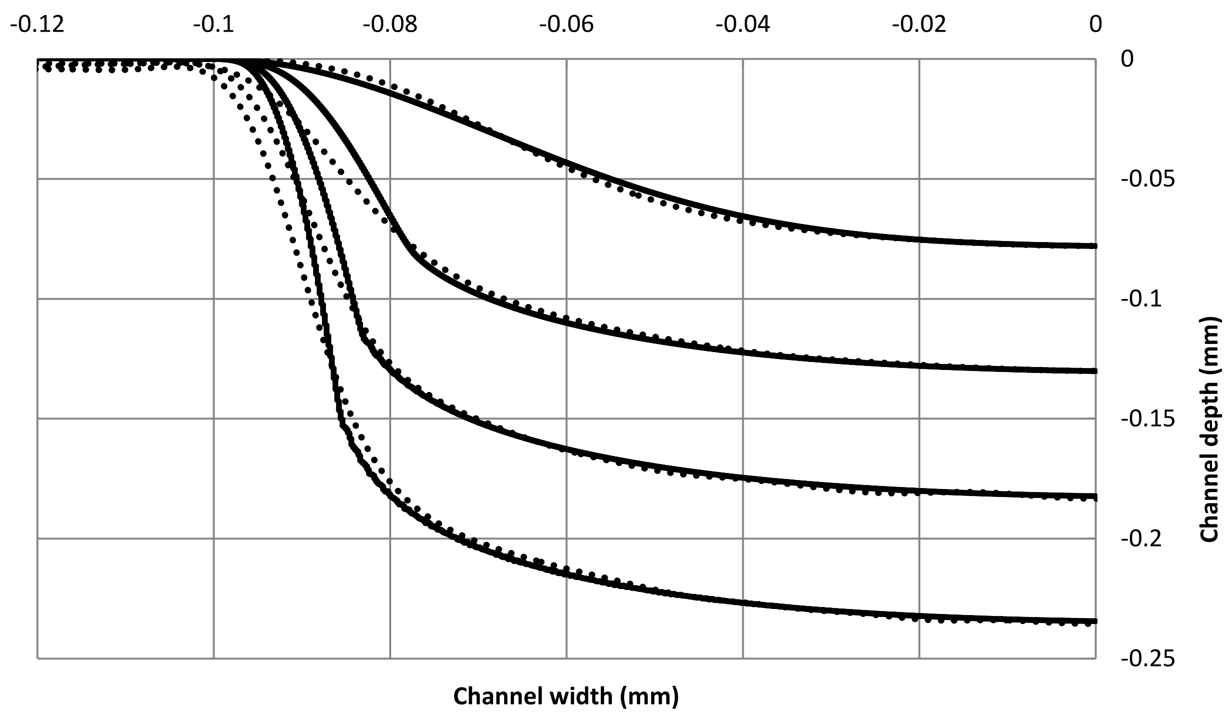

Figure 7-4: Comparison of the predicted (solid lines) and measured (dots) profiles of masked channels in 316L stainless steel at α=90° for 1, 3, 5, 7 and 9 passes. One half of a symmetric channel is shown. The mask edge was located at x = -0.1. The third-pass experimental profile was used as the erosive efficacy in the form of Q $(x) = 0.39\,\frac{(-1+e^{(-20(x+0.5)^2)})}{-(-1+e^{(-20(0.5)^2)})}$.

Figures 7-2 – 7-4 show the channel cross-sectional profiles predicted by Eq. (4-1) solved using an initial condition of $z(x, 0) = 0$ for the masked machining of the three metals. The center-line depths of all three metals were predicted accurately (within 3%) up to an aspect ratio of approximately 1.25. On average, the channel shapes were also predicted quite well, with the relatively flat channel bottoms and steep sidewall slopes characteristic of the AJM of ductile polymers [12]. In addition, the profiles showed minimal mask under-etching in the case of the aluminum alloy and stainless steel (<10 µm), while under-etching was much more pronounced for the case of the titanium alloy (20 µm), notably as the channel depth increased. While modeling the surface evolution, it was noted that channel width predictions were very sensitive to the fit of angular impact erosion dependence, *g(α),* and care must be taken to insure accurate data is obtained.

Chapter 8: Conclusions and Recommendations

8.1 Summary

This investigation is to the author's knowledge the first attempt in modeling the surface evolution for application in the abrasive jet micro-machining of metals. Presented below is a summary of what was accomplished in this study.

The erosion rates of aluminum 6061-T6, 316L stainless steel and Ti-6Al-4V alloy were measured. This was done by machining channels with an abrasive jet and measuring the volume loss using a profilometer. From this, the angular dependence of erosion for the metals was derived. As expected for ductile materials, the maximum erosion rate occurred between impact angles of 20°-30°. Thus ductile erosion governs the process, and the mechanisms of erosion are cutting at lower angles and deformation at impact angles approaching normal.

The angular dependence was fit to the empirical model of Oka et al. [18]. On a volumetric basis, it was found that 316L stainless steel had the highest erosion resistance, followed by Ti-6Al-4V alloy and then aluminum 6061-T6. Previous researchers attempted to correlate erosion with yield and ultimate tensile stresses, toughness, uniform strain and ductility. In the present study, only elastic modulus and fracture toughness were found to be vaguely related to the erosion rate, while the extent of particle embedding in each metal did not correlate with erosion. When combined, these properties yield the strain energy release rate, the energy required to produce a unit crack extension. This correlated well with the order of the erosion rates between the three metals.

The angular dependence of erosion was then used as an input to a previously derived surface evolution model for ductile metals [13]. The cross-sectional shapes of unmasked channels machining at normal incidence were predicted accurately in aluminum alloy. In the case of oblique incidence (i.e., nozzle inclined in the plane transverse to the channel axis), a novel coordinate transformation for the erosive efficacy was derived which allowed accurate prediction of asymmetric unmasked channels in aluminum, with a maximum error in the center depth of approximately 4% at an aspect ratio approaching 0.1.

The surface evolution model was also applied to masked channels for aluminum 6061-T6, 316L stainless steel and Ti-6Al-4V alloy machined at normal incidence. A modification to the model was made in estimation of the erosive efficacy of the jet to account for the mask scattering effect. The center-line depths were quite accurately predicted up to an aspect ratio of approximately 1.25, with a small discrepancies caused by the first order erosive efficacy approximation.

The use of the first or third pass profile proved successful in modeling the erosive efficacy in unmasked channels. A first order iterative technique used to estimate the erosive efficacy of the jet for masked channels proved rather difficult to solve due to its sensitivity to the impact angle dependence of erosion and steep sidewall slopes. Thus care must be taken to ensure this data is obtained accurately in order for the model to accurately predict channel width. Therefore knowledge of the velocity and flux for unmasked and masked channels was not required for the use of this model for surface morphology prediction.

Particle embedding was easily noted in the 316L stainless steel and Ti-6Al-4V substrates through examination under the SEM. However, a particle tagging technique in conjunction with viewing masked channels under the SEM proved that the presence of embedded particles in aluminum, but its distribution was difficult to quantify. An erosion – velocity relationship was observed with velocity exponents of 3.44, 2.21 and 2.04 for aluminum, stainless steel and titanium alloys respectively.

8.2 Conclusions

The major findings and contributions of this thesis were as follows:

1. The angular dependence of erosion indicated a ductile erosion response with maximum erosion occurring between 20-35° for aluminum 6061-T6, 316L stainless steel and Ti-6Al-4V when eroded with 50μm Al_2O3_3 abrasive.
2. The most resistant metal to erosion was 316L stainless steel, followed by Ti-6Al-4V and then by aluminum 6061-T6. This correlated roughly with the strain energy release rate.
3. The surface evolution model predicted unmasked symmetric and asymmetric channel cross-section profiles in aluminum 6061-T6 accurately using a novel coordinate transformation to estimate the erosive efficacy.

4. The surface evolution model accurately predicted the cross-sectional profile of masked channels in aluminum 6061-T6, 316L stainless steel, and Ti-6Al-4V alloy by modifying the model to account for the mask scattering effect.
5. Evidence of particle embedding was noted in varying quantities for all three metals.

8.3 Implications for industry

AJM is a clean, cheap, simple and a proven alternative in the manufacturing of micro-components. While its direct use on brittle materials for MEMs and micro-fluidics are apparent, this research establishes a new means for its use on metals in many industries. Direct advantages of using metals in micro-components are increased strength, ductility, conductivity and material availability.

There is potential use for metallic micro-components in the biomedical industry, such as implants. As technology encourages the downsizing of components to ever shrinking levels, the micro-machining of metals using cheaper AJM techniques will become a viable alternative than micro-milling or laser cutting. This is especially true for 316L stainless steel and Ti-6Al-4V alloys, which are already being used in the biomedical field.

The robotic industry also may have use for miniature metal products, machined using AJM techniques. Technological advancements will now demand smaller components for use in sensors, drive-trains and power sources on the micron scale. The availability and capacity of AJM to create such components will become a viable and meaningful solution in their production.

There are however, some disadvantages to using this technique in industry. Compared to conventional milling, and newer techniques such as laser beam machining and water-jet machining, AJM in metals is rather slow. A maximum erosion rate of 0.0014 g/g was found in 316L Stainless steel, while Getu et al. [12] found a maximum erosion rate of 0.0035 g/g for polymethylmethacrylate using 25μm abrasive. Since its material removal mechanism is predominantly erosion, its etch rate depends heavily on material properties such as hardness, unlike electron beam machining [6 - 7]. While equipment costs are still relatively low, care must be taken through proper ventilation equipment to protect users from inhaling air-born abrasive and target material dust, especially when machining hazardous targets such as beryllium copper [48].

8.4 Recommendations for Future Work

Preliminary work such as basic erosion rate modeling and surface evolution of micro-channels of metals has been conducted in this thesis. However, much remains to be investigated in this area, in order for the AJM of metals to become a competitive and viable manufacturing process. Specifically:

- Investigate the surface finish after the AJM of metals, such as hardness, roughness, consistency and surface integrity, and possible post-processing techniques for improvement. This is important for surface-sensitive applications, such as micro-molds.
- Study the effect of particle embedding on the surface, its importance, and to better quantify the amount of embedded particles.
- Modify the model to account for limitations such as the mask edge effect, particle embedding, rebounding particles and its sensitivity to steep sidewalls. In particular, a fix for the sensitivity to impact angle dependence could be implemented, and efficiencies could be found to reduce solving time.
- Develop a model for the AJM of metals for planar and transitional areas, micro-holes and suspended structures, for use in machining components with varying proportions and features.
- Examine the effect of an oblique jet on masked channel machining and the scanning direction to determine more efficient means of material removal and surface finish.
- Explore other metals for use in industry such as copper, brass, silver, gold and steels, noting if its modeling pattern follows the effect of the investigated aluminum, stainless steel and titanium alloys.

Appendices

Appendix A: The Effect of Cryogenics on the Erosion of 316L Stainless Steel

Urbanovich and Kramchenkov [40] investigated the erosion of steels and alloys at temperatures of 80-293K and noted a shift in the erosion rate versus angle relationship possibly due to the material becoming brittle. In recent work, a cryogenic setup was developed to cool the target material for the AJM of elastomers such as polydimethylsiloxane (PDMS) [14]. Using cryogenic temperatures while performing other machining operations such as grinding is known to generate lower roughness, fewer defects, higher work hardening and less tensile residual stresses [49]. It was thus of interest to explore whether this technique could also offer such advantages in the AJM of 316L stainless steel.

A cryogenic setup was used to pressurize liquid nitrogen at 30 psi, shown in Figure A-1. A tank holds the boiling nitrogen, which is released through a valve, exiting a jet, cooling the substrate surface. All blasting parameters were similar to those mentioned in Chapter 3, including a feed rate of 0.3 mm/s and nozzle standoff of 20 mm. The blasting pressure of the 50µm aluminum oxide abrasive was kept at 400 kPa, yielding a particle velocity of 106 m/s. The liquid nitrogen was allowed to flood the surface of the stainless steel substrate while being blasted by the abrasive jet at normal impact. This ensured that the surface temperature remained at -196°C during blasting.

Figure A-1: The cryogenic apparatus used to dispense the liquid nitrogen onto the substrate.

Various channel depths were achieved by machining 2, 3 and 4 passes of the jet. Limitations in the apparatus did not allow for slower feed rates or more jet passes. The stainless steel was allowed to warm up before machining a similar channel without the cryogenic jet for comparison. Samples were then blown off with compressed air, and measured with the profilometer to determine mass loss. Figure A-2 is a plot of mass loss versus dosage at both cryogenic and non-cryogenic temperatures in stainless steel.

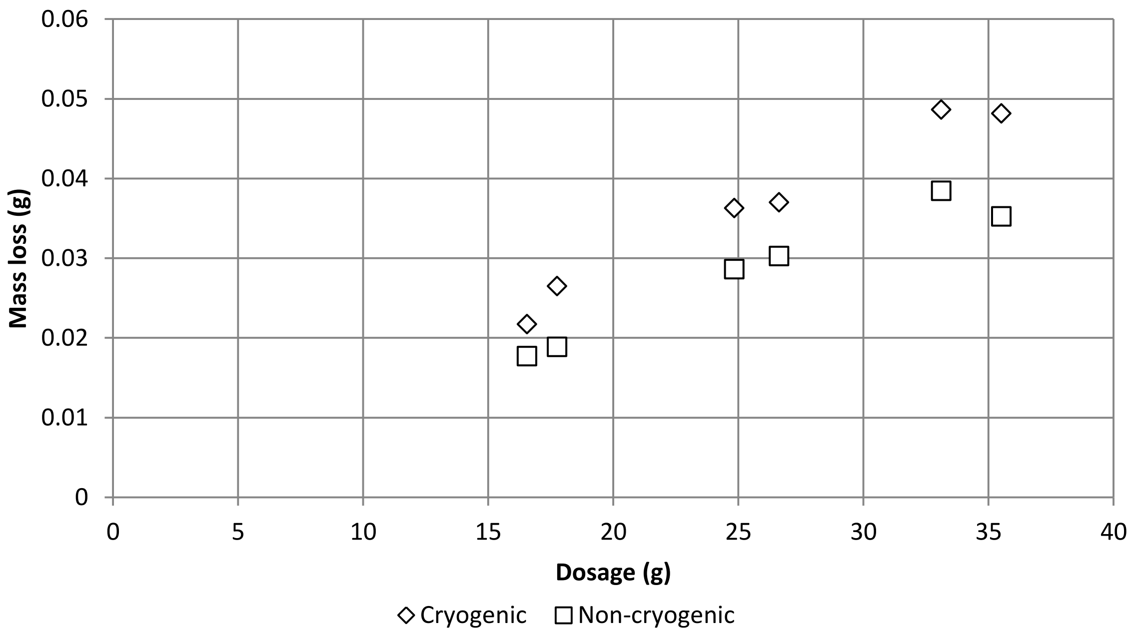

Figure A-2: Mass loss versus dose for 316L stainless steel at normal impact with and without the cryogenic jet cooling the surface.

The effect shown in Figure A-2 is a slightly higher erosion rate at normal impact due to the embrittlement of the stainless steel substrate at lower temperatures. However, the gain is rather small (~ 20%) for the effort undertaken to produce these results. The effect of cryogenic cooling on the surface profiles is shown in Figure A-3.

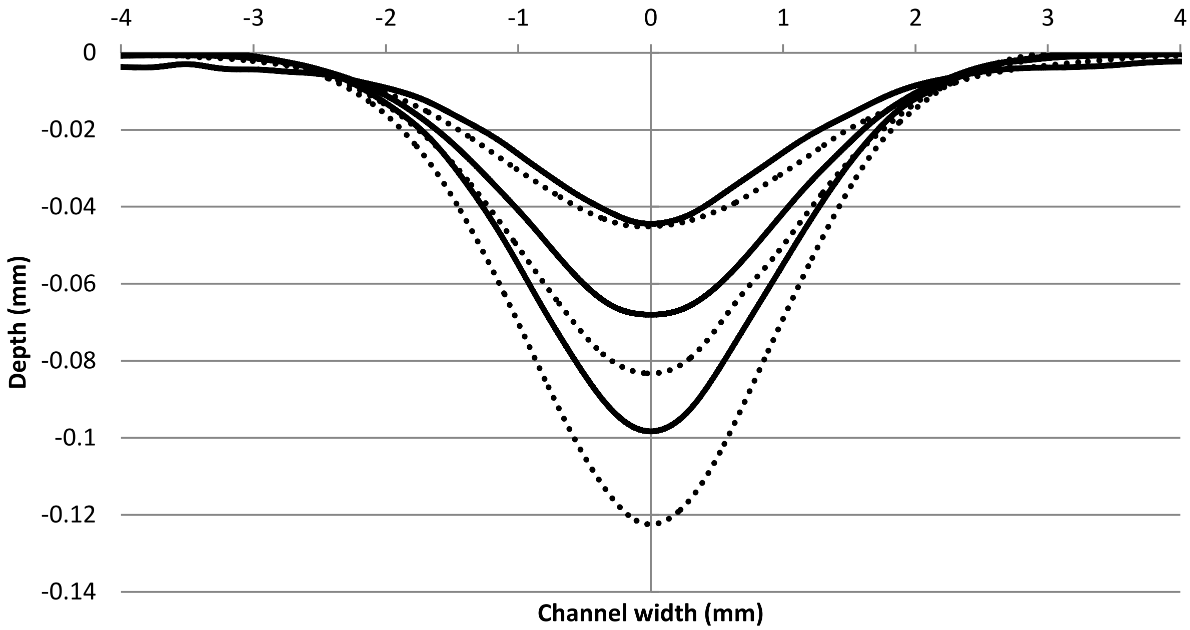

Figure A-3: The effect of cryogenic cooling on the surface profiles for 2, 3 and 4 passes of the abrasive jet. Solid lines indicate room temperature machined profiles and dashed lines indicate cryogenically cooled channel profiles.

As both Figures A-2 and A-3 attest, the difference between cryogenically assisted and room temperature AJM for stainless steel is rather small. There is no difference in the shape of the profile, as shown in Figure A-3, with a maximum difference in depth of ~ 25%. From the standpoint of micro-machining, a deeper depth profile could simply be achieved by using a higher dose of abrasive; however the resulting surface finish is yet to be studied.

Appendix B: Investigation of Particle Embedding

The embedment of particles in the surface of a metal during abrasive jet micro-machining is important because the embedded particles could cause an increase in surface roughness, surface hardness and potentially a decrease in the integrity of the material or feature. In many cases, depending on the erodent, it is nearly impossible to remove or dissolve embedded particles through a post-processing technique after machining. Particle embedding generally depends on the material properties and the blasting conditions, and as discussed in section 2.4.2, many researchers have found embedded particles on the surface after machining. This appendix highlights some of the techniques used in this study to identify erodent embedded in the substrate.

B.1 Scanning electron microscopy

Using an elemental energy-dispersive X-ray spectroscopy (EDX), or scanning electron microscopy (SEM) analysis, the aluminum oxide erodent used in the AJM experiments was difficult to distinguish using from the aluminum oxide on the surface of the aluminum 6061-T6. It was initially thought that the ceramic abrasive would have been easily distinguished by a notably larger peak in oxygen content when a machined surface was viewed under a scanning electron microscope (SEM). However, oxygen isn't a reliable measurement on the SEM equipment because aluminum and oxygen are relatively close to each other on the periodic table.

The backscatter sensor on the SEM detects surface composition just beneath the surface (1 μm). It was thought that if a 50 μm particle embedded itself on a machined surface, it would show up as a high oxygen concentration, since there is no oxide beneath just beneath the surface. However, since the surface was rather rough, the use of backscatter did not provide any conclusion as to the amount of particles embedded.

B.2 Examination using optical microscope

Visually looking at the machined aluminum substrate under a microscope did not distinguish embedded particles either. A microscope (Clemex PS3 Research System, Clemex Technologies Inc., Longueil, Quebec, Canada) was used to aid in optically distinguishing the embedded particles. Using a larger, 150 μm particle size did not help in physically identifying embedded particles because surface was too rough in the channel after machining.

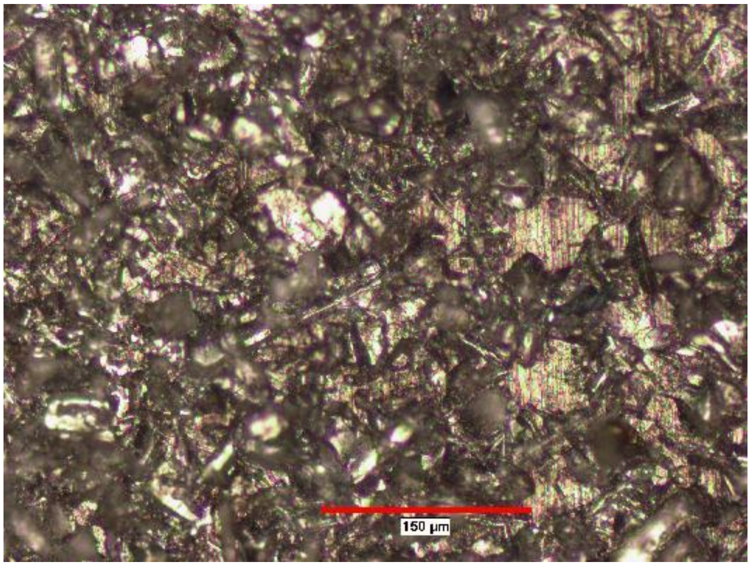

Figure B-1: Microscope image of the blasted surface of a channel in aluminum. Note how the limited depth of focus indicates craters and peaks, though it is hard to conclude on the presence of particles.

B.3 Cross-sectioning method

It was then hypothesized that a cross-sectional SEM view of the blasted samples might reveal the presence of embedded particles, if compared to a fresh aluminum surface. This was attempted using two methods. First, an aluminum sample was cross-sectioned and its edges were milled flat to ensure a sharp edge. Next, the pieces were butt-jointed together and a channel was machined across the joint. The pieces were pulled apart for examination of the cross-sections under the SEM. Unfortunately, since the aluminum almost instantly formed an oxide layer and the SEM's oxygen detection isn't reliable, only a slight increase in oxygen content was noted near the machined surface. Since the milling operation isn't perfect, a slight fillet was noted at the edge where the two sections met, and some abrasive penetrated the butt-joint, as shown in Figure B-2.

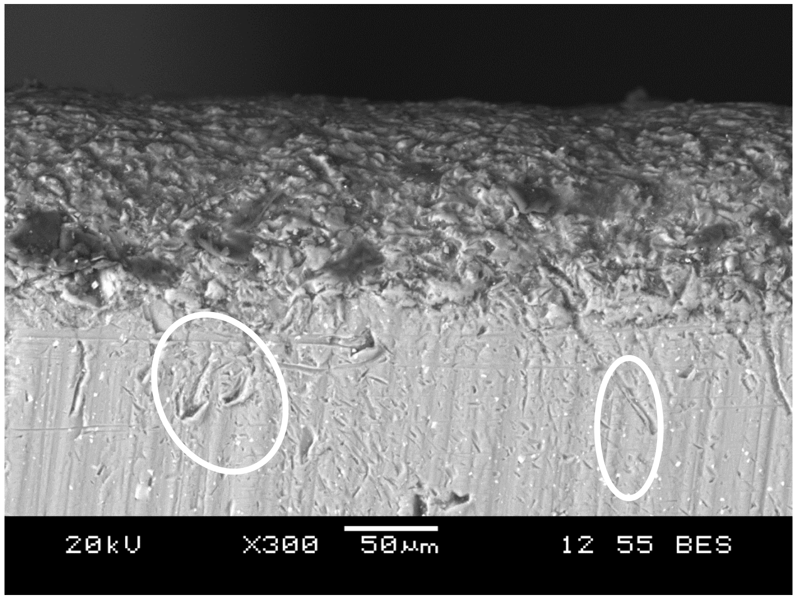

Figure B-2: SEM back scatter image of the cross-section of a machined channel in aluminum. Encircled are the areas where abrasive penetrated the butt-join.

The cross-sectioning method was also attempted after machining a channel in the aluminum sample. The sample was sectioned and polished while encased in Lucite to protect its edges from rounding during standard polishing. However it was noted under an optical microscope that any embedded particles would likely be knocked off during the polishing operation, and thus this method was deemed futile.

B.4 Incubation period

An incubation period occurs when initially the substrate gains weight due to the embedment of particles, after which mass is lost through normal erosion. By varying the number of passes of the abrasive jet, a small controlled dosage was achieved, however no samples showed weight gain, as shown in section 5.1.

B.5 Roughness measurements

Another indication of particle embedding might be seen in changes in roughness. It was thought that since particles are relatively large (50 µm) compared to the unmasked channel depth (Figure 6-2 – 6-4) (20-150 µm), embedded particles protruding above the surface would cause an adverse affect on roughness. However as will be demonstrated in Appendix C, the roughness as a function of dose did not vary that much.

B.6 Particle tagging

Since optically or chemically distinguishing embedded aluminum oxide particles in an aluminum 6061 substrate did not prove conclusive, a particle tagging technique was pursued. A number of different particle tags were proposed: salt, iodine, fabric die, gentian violet, potassium permangate, bromothymol blue and pen ink. It was thought that these substances could act as a physical or chemical tag that can be used to identify abrasive embedded within the aluminum under the SEM or microscope, if they stuck to the particles after machining.

The saturated salt water, fabric die, iodine, gentian violet and ink were dissolved in measured quantities of water and mixed with abrasive. The abrasive slurry was then baked overnight to dry out the water content, with the tag supposedly sticking to the particle to be identified by. After baking, no traces of iodine were found in the abrasive, thus the iodine – abrasive solution was dissolved using an alcohol solution instead and allowed to evaporate.

Channels were blasted in aluminum samples with the chemically coated abrasives at normal impact. After blown with compressed air, the samples were examined under the SEM for the chemical tags on the abrasive. Only the salt-coated abrasive was detected on the blasted surface by the SEM, but it resulted in a sparse, uneven distribution on the EDX map, and unfortunately did not provide a solid quantification of the amount of abrasive embedded on the surface. Unfortunately, no solid chemical evidence of the other abrasive tags could be found on the blasted surface, implying either there were no embedding particles, or the abrasive coat was rubbed off during the blasting process. The SEM image in Figure B-3 revealed that the chemical tag was not coating the entire surface evenly to begin with. Figure B-4 is the EDX map of the machined surface with salt-coated particles.

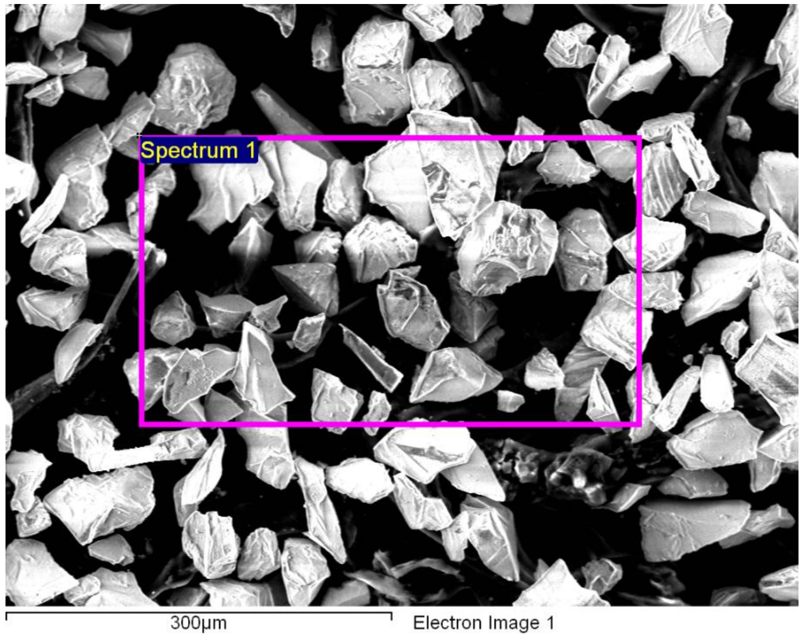

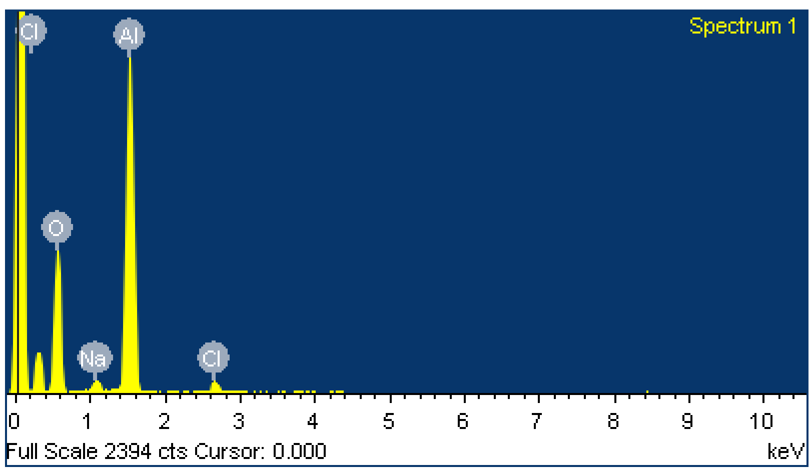

Figure B-3: EDX map of the salt coated particles. Note the relatively low concentration of NaCl content indicating uneven coverage of the abrasive by the salt solution.

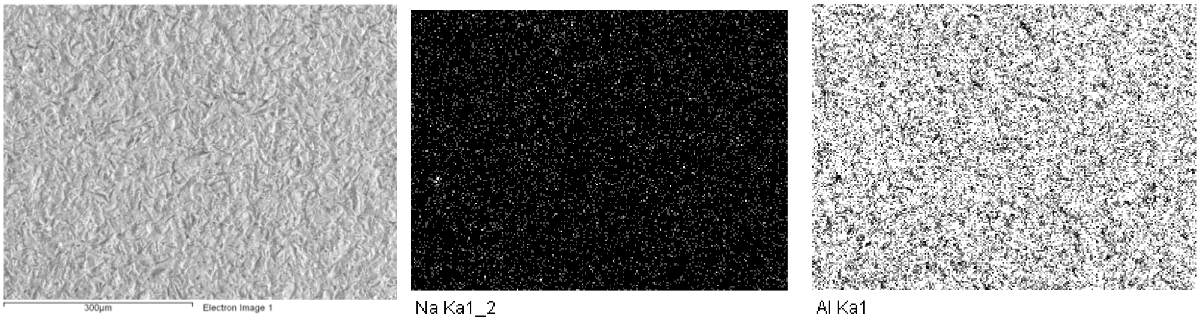

Figure B-4: EDX map of a machined channel in aluminum using salt-coated particles, showing original SEM image (left), sodium content (centre), and aluminum content (right).

Since chemically distinguishing particle tags did not conclusively demonstrate embedded particles, samples were examined under the microscope in an attempt to distinguish them from the surrounding substrate. In particular, the blasted surfaces when the purple fabric die and ink coated particles were examined because of their dark, contrasting color with the background. Images show some evidence of colored particles embedded within the surface. However since not all particles were coated evenly, there could be many untagged embedded particles. Figure B-5 shows images of purple fabric die and ink coated particles embedded in an aluminum channel. Particle density was approximately one particle every 3 mm^2.

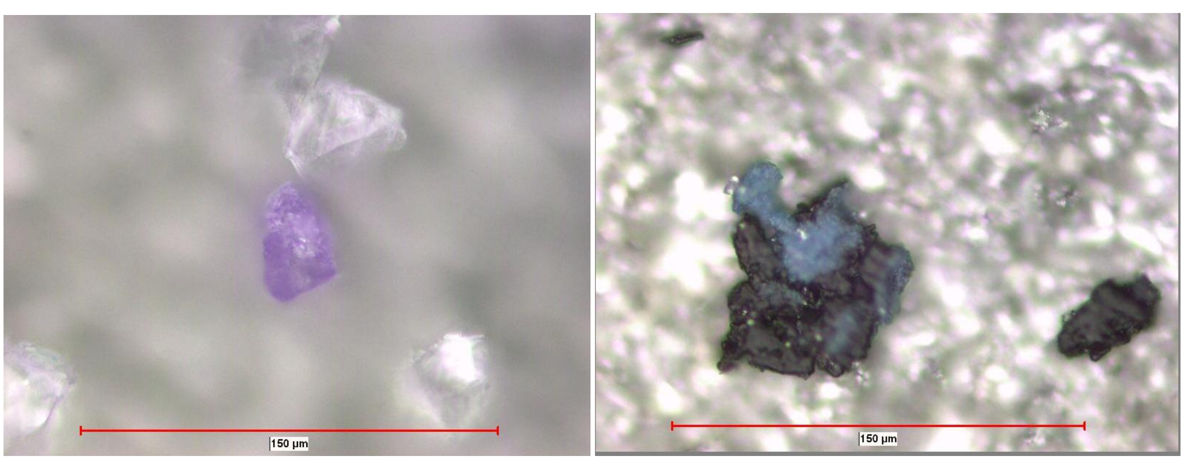

Figure B-5: A microscope image of a channel blasted in aluminum with fabric die (left) and ink (right) coated particles.

B.7 Cross-section of a masked channel

After machining, a masked channel was cross-sectioned and polished to be examined under the SEM. While obtaining images of masked channels, it was noticed that there were particles protruding from the channel surface. It was confirmed by the EDX that these were in fact aluminum particles of varying sizes and special distribution, as opposed to some dirt or dust. This added valuable evidence for the argument of particle embedding in aluminum after AJM. Figure B-6 shows an image of such particles in a masked channel.

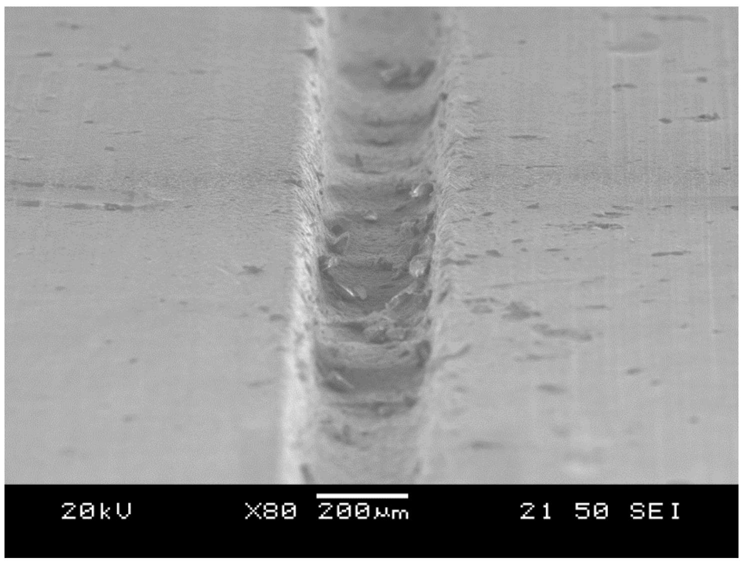

Figure B-6: An SEM image of a masked channel machined in aluminum after five passes of the jet at 0.3mm/s feed rate at normal impact. Particles are seen protruding from the machined surface, confirmed to be aluminum with the EDX.

To conclude, by summing the evidence from the methods above, an argument could be formed that aluminum oxide abrasive are embedding during the AJM of aluminum 6061 T6. The coated abrasives in addition to the SEM image of the masked channel demonstrated that there were indeed embedded particles in the aluminum substrate; however the amounts were difficult to quantify. Such a problem did not exist in distinguishing particles from the substrate for the 316L stainless steel and Ti-6Al-4V alloy as they were easily highlighted on the SEM, as discussed in section 5.3.

Appendix C: Channel center roughness

A brief study was undertaken to obtain data for the roughness along the centre of the machined channels. Depending on the final application, it may be important to know the surface roughness of a machined channel, especially if it will directly affect the outcome of another product, such as in micro-molds. Moreover, roughness could also reveal clues to the mechanisms of erosion and degree of particle embedding occurring in the target material during the AJM process.

The optical profilometer was used to measure the roughness of the channel. First, a cross-section profile was measured to align the stylus with the centre of the channel. The roughness along the length of the center of the channel was measured in 2 mm increments, at a scan rate of 0.1mm/s. Using the analysis software, the roughness value, Ra was calculated in accordance to ISO 4287, Geometrical Product Specifications – Surface texture: Profile method [51]. This was done for aluminum 6061-T6, 316L stainless steel and Ti-6Al-4V alloy at normal and 45° impact angles, with blasting conditions the same as in Chapter 3 for stepped channels. The results are presented in Figures C-1 and C-2.

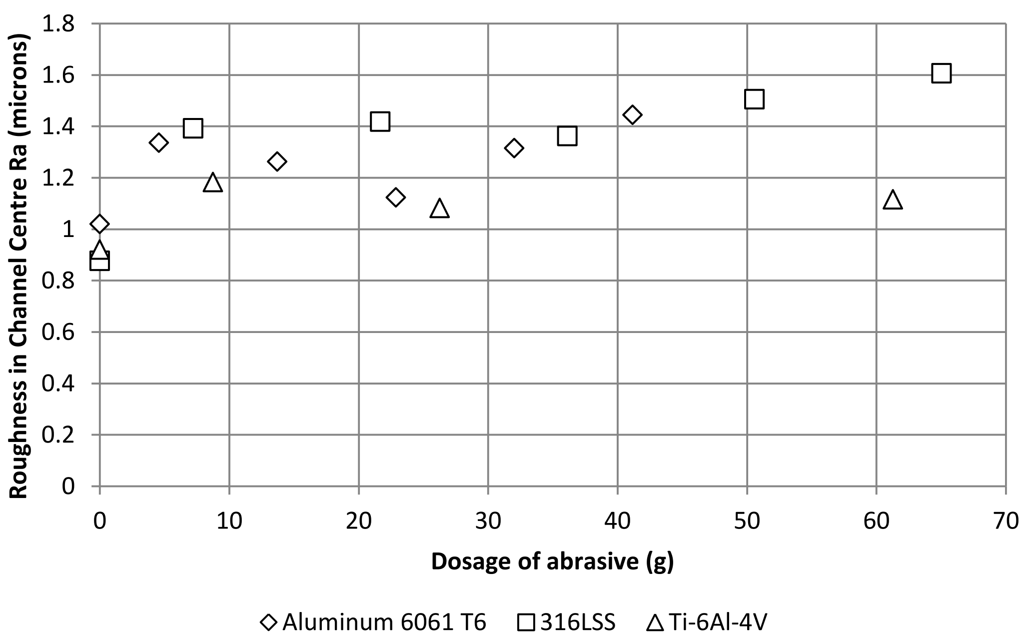

Figure C-1: Roughness along the center of the channel versus dose for the three metals machined at normal impact.

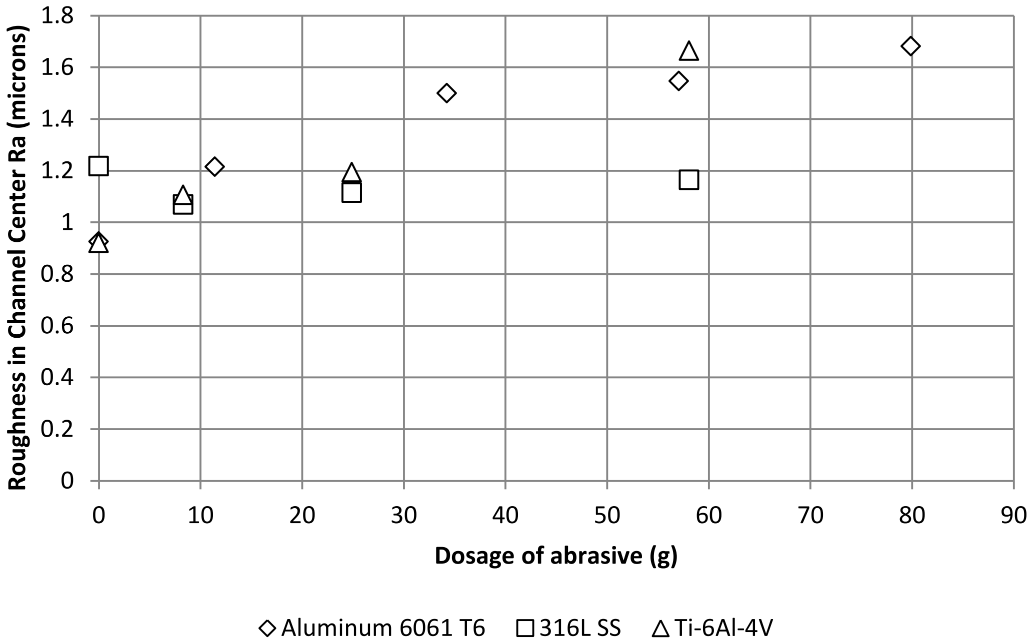

Figure C-2: Roughness along the center of the channel versus dose for the three metals machined at 45° impact.

It was expected that the surface roughness would increase initially at low dosage during the erosion process, and then level off at a steady state. At normal impact, it is evident from Figure C-1 that increases in surface roughness occurred within the first pass (second data point), for all three metals. Additionally, the aluminum and stainless steel substrates have somewhat similar roughness throughout, while titanium has a notably smoother machined surface. This correlates well with the hardness values of these metals, where aluminum and stainless steel have a measured hardness of 0.11 GPa and 0.14 GPa respectively, while titanium has a hardness of 0.318 GPa, making it much harder to indent.

At 45° however, both titanium and aluminum showed an increase in the roughness as a function of the dose, while the stainless steel roughness stayed relatively constant. This could relate to the stainless steels' superior erosion resistance, as was discussed in Chapter 5.

Appendix D: Velocity exponents

The determination of velocity exponent was outlined in section 3.5, and its results were presented in section 5.4. Figure D-1 – D-3 illustrates the erosion versus velocity graphs that were used in obtaining these velocity exponents.

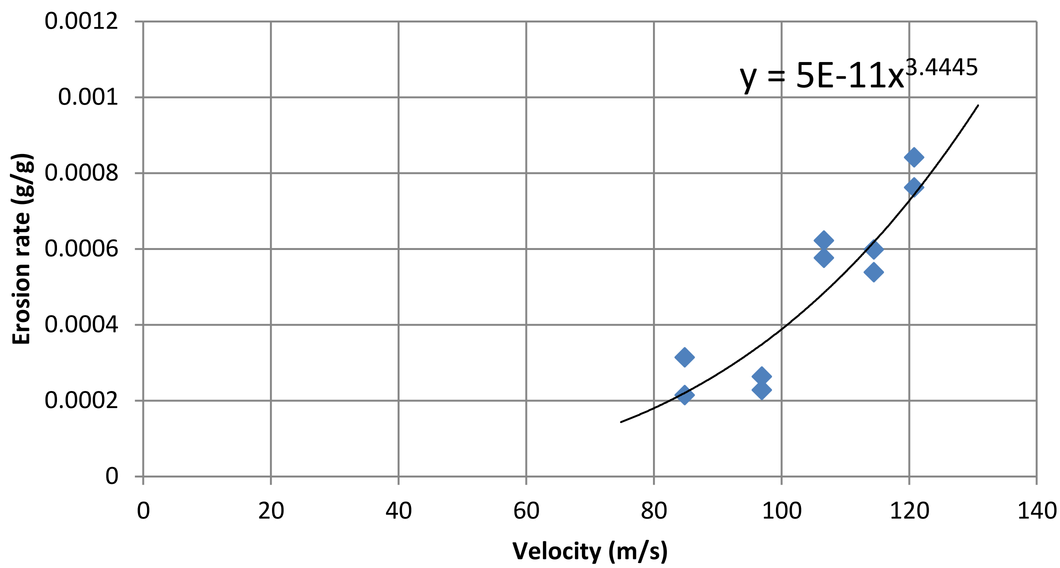

Figure D-1: The erosion rate versus velocity relation for aluminum 6061-T6. The velocity exponent is 3.44.

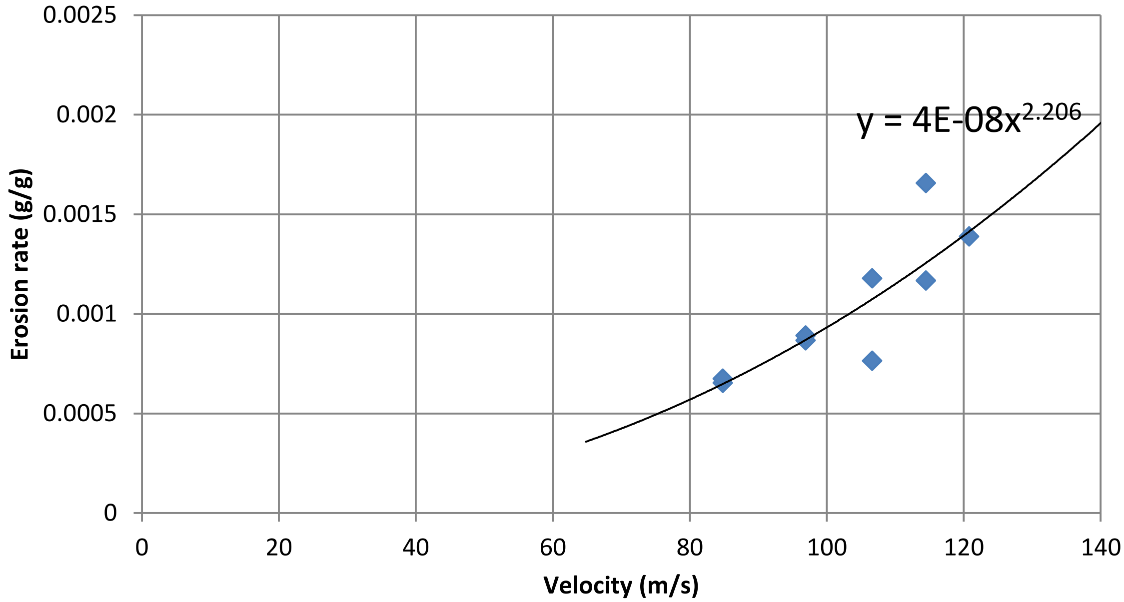

Figure D-2: The erosion versus velocity relation for 316L stainless steel. The velocity exponent is 2.21.

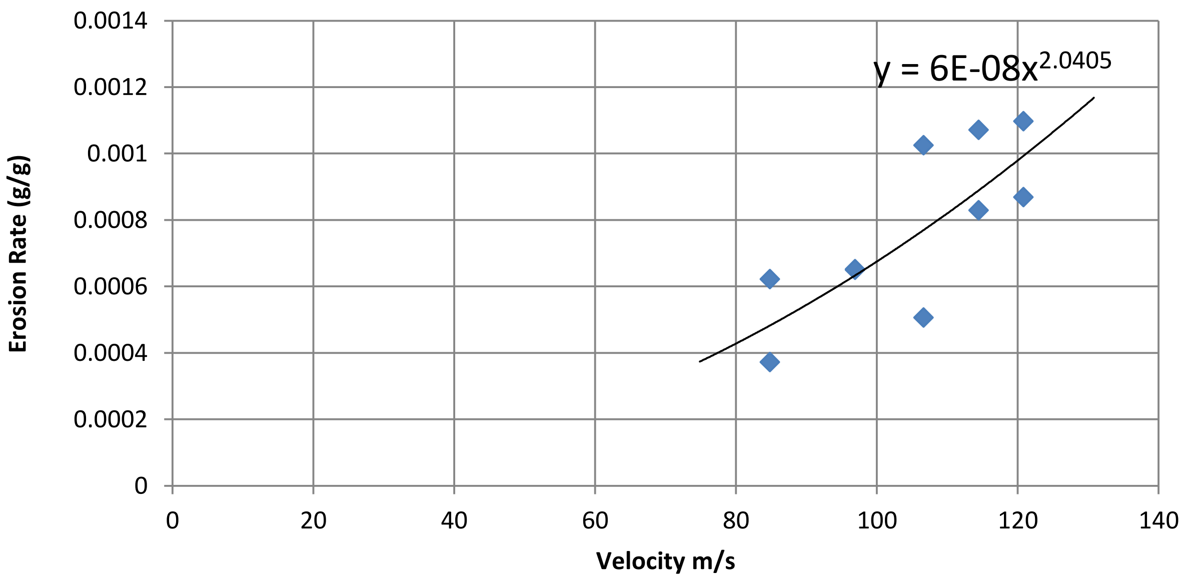

Figure D-3: The erosion versus velocity relation for Ti-6Al-4V alloy. The velocity exponent is 2.04.

References

[1] *PCB Manufacturing Process*. (n.d.). Retrieved 10 28, 2011, from Radio Electronics.com: http://www.radio-electronics.com/info/manufacture/manufacture/pcb/pcb-manufacturing-process.php

[2] *The Significant Advantages of Our Chemical Etching Precision Metal Milling Services*. (n.d.). Retrieved 10 28 2011, from Fotofab: http://www.fotofab.com/cmp_advantage.php

[3] *Wet Etching*. (n.d.). Retrieved 10 28 2011, from Siliconfareast: http://www.siliconfareast.com/wetetch2.htm

[4] *ECM Technology: Pros and Cons*. (n.d.). Retrieved 10 28, 2011, from ECM Technologies: http://www.electrochemicalmachining.com/ecm/pros-and-cons

[5] *Advantages and Disadvantages of ECM*. (n.d.). Retrieved 10 28, 2011, from Scribd: http://www.scribd.com/doc/59222416/70/Advantages-and-disadvantages-of-ECM

[6] *Electron Beam Machining (EBM)*. (n.d.). Retrieved 10 28, 2011, from: http://www.slideshare.net/a.b1986/ebm-1402113

[7] *What Is Electron Beam Machining?* (n.d.). Retrieved 10 28, 2011, from WiseGeek: http://www.wisegeek.com/what-is-electron-beam-machining.htm

[8] *Abrasive Jet Machining*. (n.d.). Retrieved 10 10, 2011, from ASM Interational: http://www.asminternational.org/portal/site/www/AsmStore/ProductDetails/?vgnextoid=56327e0e64e18110VgnVCM100000701e010aRCRD#details

[9] Ghobeity, A., Krajac, T., Burzynski, T., Papini, M., Spelt, J.K. (2007). Surface evolution models in Abrasive Jet Micromachining. *Wear* 264, 185-198

[10] Burzynski, T., Papini, M. (2010). Level set methods for the modelling of surface evolution in the abrasive jet micromachining of features used in MEMS and microfluidic devices. *Journal of Micromechanics and Microengineering* 20.

[11] D.S. Park, M. C. (2003). Mechanical etching of micro pockets by powder blasting. *The International Journal of Advanced Manufacturing Technology* 25, 1098-1104.

[12] Getu, H., Ghobeity, A., Spelt, J.K., Papini, M. (2007). Abrasive jet micromaching of polymethylmethacrylate. *Wear* 263, 1008-1015.

[13] Getu, H., Ghobeity, A., Spelt, J.K., Papini, M. (2008). Abrasive jet micromachining of acrylic and polycarbonate polymers at oblique angles of attack. *Wear* 265, 888-901.

[14] Getu, H., Spelt, J.K., Papini, M. (2008). Cryogenically assisted abrasive jet micromachining of polymers. *Journal of Micromechanics and Microengineering 18* , 115010.

[15] Ghobeity, Spelt, J., Papini, M. (2009). Abrasive jet micro-machining of planar areas and transitional slopes in glass using target oscillation. *Journal of Materials Processing Technology* 209, 5123-5132.

[16] Liu, C., Chen, J., Engel, J., Zou, J., Wang, X., Fan, Z., Ryu, K., Shaikh, K., Bullen, D. Polymer micromachining and applications in sensors, microfluidics, and nanotechnology, in: The 226th National Meeting of the American Chemical Society (ACS), New York, NY, September 11-17 2003.

[17] Veerabhadra Rao, P., Young, S., Buckley, D. (1983). Morphology of an aluminum alloy eroded by a normally incident jet of angular erodent particles. *Wear* 92 , 31-49.

[18] Oka, Y., Ohnogi, H., Hosokawa, T., Matsumura, M. (1997). The impact angle dependence of erosion damage caused by solid particle impact. *Wear* 203-204, 573-579.

[19] Oka, Y., Okamura, K., Yoshida, T. (2005). Practical estimation of erosion damage caused by solid particle impact. *Wear* 259, 95-101.

[20] Neilson, J., Gilchrist, A. (1967). Erosion by a stream of solid particles. *Wear* 11, 111-122.

[21] Emiliani, M., Brown, R. (1984). The effect of microstructure on the erosion of Ti-6Al-4V by spherical particles at 90° impact angles. *Wear* 97, 323-338.

[22] Yerramareddy, S., Bahadur, S. (1991). Effect of operational variables, microstructure and mechanical properties on the erosion of Ti-6Al-4V. *Wear* 142, 253-263.

[23] Harsha, A.P., Bhaskar, Deepak Kumar. (2008). Solid particle erosion behavior of ferrous and non-ferrous materials and correlation of erosion data with erosion models. *Materials and Design* 29, 1745-1754.

[24] Singh, T., Tiwari, S.N., Sundararajan, G. (1990). Room temperature erosion behavior of 304, 316 and 410 stainless steels. *Wear* 145, 77-100.

[25] Morrison, C.T., Scattergood, R.O., Routbort, J.L. (1986). Erosion of 304 stainless steel. *Wear* 111, 1-13.

[26] O' Flynn, D.J., Bingley, M.S., Bradley, M.S.A., Burnett, A.J. (2000). A model to predict the solid particle erosion rate of metals and its assessment using heat-treated steels. *Wear* 248, 162-177.

[27] Oka, Y.I., Okamura, K., Yoshida, T. (2005). Practical estimation of erosion damage caused by solid particle impact Part 1: Effects of impact parameters on a predictive equation. *Wear* 259, 95-101.

[28] Rodriguez, E., Flores, M., Perez, A., Mercado-Solis, R.D., Gonzaliez, R. (2009). Erosive wear by silica sand on AISI H13 and 4140 steels. *Wear* 267, 2109-2115.

[29] Sapate, S.G., Rama Rao, A.V. (2002). Effect of material hardness on erosive wear behavior of some weld-deposited alloys. *Materials and Manufacturing Processes*, 17(2), 187-198.

[30] Shipway, P.H. (1996). The effect of plume divergence on the spatial distribution and magnitude of wear in gas-blast erosion. *Wear* 205, 169-177.

[31] Finnie, I., McFadden, D.H. (1978). On the velocity dependence of the erosion of ductile metals by solid particles at low angles of incidence. *Wear* 48, 181-190.

[32] Cousens, A.K., Hutchings, I.M. Proc. Int. Conf. on Erosion by liquid and solid impact. (1983).

[33] Meng, H.C., Ludema, K.C. (1995). Wear models and predictive equations: their form and content. *Wear* 181-183, 443-457.

[34] Reshetnayak, H., Kuybarsepp, J. (1994). Mechanical properties of hard metals and their erosive wear resistance. *Wear* 177, 185-193.

[35] Ambrosini, L., Bahdur, S. (1987). Erosion of AISI 4140 steel. *Wear* 117, 37-48.

[36] Oka, Y.I., Yoshida, T. (2005). Practical estimation of erosion damage caused by solid particle impact Part 2: Mechanical properties of materials directly associated with erosion damage. *Wear* 259, 102-109.

[37] Malkin, S. (1981). Correlation between solid particle erosion of metals and their melting energies. *Wear* 68, 391-396.

[38] Ghobeity, A., Getu, H., Krajac, T., Spelt, J., Papini, M. (2007). Process repeatability in abrasive jet micro-machining. *Journal of Materials Processing Technology* 190, 51-60.

[39] Li, H., Wang, J., Fan, J. (2009). Analysis and modelling of particle velocities in micro-abrasive air jet. *International Journal of Machine Tools & Manufacture* 49, 850-858.

[40] Papini, M., Ciampini, D., Krajac, T., Spelt, J.K. (2003). Computer modelling of interference effects in erosion testing: effect of plume shape. *Wear* 255, 85-97.

[41] *Aluminum 6061-T6; 6061-T651*. (n.d.). Retrieved 3 1, 2011, from ASM Aerospace Specification Metals Inc.: http://asm.matweb.com/search/SpecificMaterial.asp?bassnum=MA6061t6

[42] *AISI Type 316L Stainless Steel annealed sheet*. (n.d.). Retrieved 9, 1, 2011, from ASM Aerospace Specification Metals Inc.: http://asm.matweb.com/search/SpecificMaterial.asp?bassnum=MQ316N

[43] *Titanium Ti-6Al-4V (Grade 5), ELI, Annealed*. (n.d.). Retrieved 9, 1, 2011, from ASM Aerospace Specification Metals Inc.: http://asm.matweb.com/search/SpecificMaterial.asp?bassnum=MTP643

[44] Johnson, K. (2003). *Contact Mechanics.* New York , USA: The Cambridge University Press, pp. 170.

[45] Ten Thije Boonkkamp, J., Jansen, J. (2002). An analytical solution for mechanical etching of glass by powder blasting. *Journal of Engineering Mathematics* 43, 385-399.

[46] Slikkerveer, P., Veld, F. i. (1999). Model for patterened erosion. *Wear* 233-235, 377-386.

[47] Sheldon, G., Kanhere, A. (1972). An investigation of impingement erosion using single particles. *Wear* 21, 195-209.

[48] *Preventing Adverse Health Effects From Exposure to Beryllium on the Job.* (n.d.). Retrieved 10 28, 2011, from United States Department of Labor: http://www.osha.gov/dts/hib/hib_data/hib19990902.html

[48] Urbanovich, L.I., Kramchenkov, E.M. (1999). Erosion of steels and alloys in their collision with a flux of abrasive particles. *Journal of Engineering Physics and Thermophysics* 72, 519-525.

[49] Bend Fredj, N., Sidhom, H. (2006) Effects of the cryogenic cooling on the fatigue strength of the AISI 304 stainless steel ground components. *Cryogenics* 46, 439-448.

[50] ASM Interational. (1990). Metals Handbook 10th Edition Vol. 1 Properties and Selection: Irons, Steels and High Performance Alloys.

[51] I*SO 4287:1997*. (n.d.). Retrieved 10 28, 2011, from International Organization for Standardization:
http://www.iso.org/iso/iso_catalogue/catalogue_tc/catalogue_detail.htm?csnumber=10132